Modeling Aerosol Particle Deposition on a Person Using Computational Fluid Dynamics

Prepared By:
Hua Ji, Fue-Sang Lien
Waterloo CFD Engineering Consulting Inc.
534 Paradise Crescent, Waterloo, Ontario

PWGSC Contractor Number: W7702-155701/001/EDM
Contract Scientific Authority: Eugene Yee, Defence Scientist, 403-544-4605

Contract Report
DRDC-RDDC-2015-C069
April 2015

Modeling Aerosol Particle Deposition on a Person Using Computational Fluid Dynamics Final Report

Hua Ji and Fue-Sang Lien

Waterloo CFD Engineering Consulting Inc. (WATCFD)
534 Paradise Cres, Waterloo
Ontario, N2L 3G1

Phone: (519) 885-6722
Fax: (519) 208-0439
Email: huaji@watcfd.com

April 3, 2015

Final Contract Report prepared for
DRDC Suffield Research Centre
Contract number: W7702-155701/001/EDM
Technical authority: Eugene Yee, DRDC Suffield Research Centre,
(403)544-4605

ABSTRACT

The Unsteady Reynolds-Averaged Navier Stokes (URANS) approach applied in conjunction with the Eddy Interaction Model (EIM) is used here to conduct numerical simulations of aerosol particle deposition on the human form. Numerical simulation of a two-phase turbulent impinging jet flow is studied to validate the proposed methodology. The numerical deposition results are compared with some relevant experimental measurements. The results of this validation show that the standard EIM with turbulent tracking tends to overpredict the deposition efficiency. Greatly improved results were achieved by using a near-wall correction with the EIM. After the validation of the methodology, a number of detailed numerical simulations of aerosol particle deposition on a human form were conducted. Simulations were conducted for 13 aerosol particle sizes ranging from 0.1 μm to 40 μm. For each of these particle sizes, three orientations of the human form relative to the incident wind direction were simulated (viz., with the human form oriented 0, 90 and 180 degrees with respect to the direction of the incident wind). High-resolution isopleths of the deposition probability on the surface of the human form are presented. To provide the quantitative information for future applications by researchers, extensive data files have been produced, providing information on the cell area for each triangle used in the tessellation of the surface of the human form, the associated body part associated with this triangular cell, and the computed deposition probability associated the triangular cell.

Contents

List of Figures

List of Tables

Chapter 1

Introduction

This study is concerned with the prediction of the deposition of aerosol particles on the human form. The methodology utilizes computational fluid dynamics (CFD) simulations to determine the complex turbulent flow around the human form, and this information is used as the input to a Lagrangian stochastic model to predict the motion around and deposition of aerosol particles on the human form. The is done by studying the statistics of a large number of "heavy" particles, each of which is moved stochastically in the turbulent flow field (reconstructed from the CFD simulations) around the human form.

There are five mechanisms by which an aerosol particle can be deposited on a surface; namely,

1. Interception;
2. Inertial impaction;
3. Brownian diffusion;
4. Sedimentation (or gravitational settling);
5. Electrostatic attraction.

Aerosol particles of 1-30 μm in size have inertia (or mass), and they will not follow exactly the sharp streamlines in the vicinity of a bluff body. Therefore, deposition can occur as a result principally of interception and inertial impaction. Brownian diffusion is only important if the particle size is much less than 1 μm. Owing to the fact that only non-volatile aerosol particles are considered herein, the gravitational settling effect is included implicitly in our Lagrangian stochastic model (which will be described in Section 2).

The electrostatic attraction effect on particle deposition will be ignored in this study.

There are three basic steps which are required to study aerosol deposition on the human form:

1. construction of an accurate grid (mesh) to represent the human form;

2. computation of the complex flow fields around the human form using the Reynolds-Averaged Navier Stokes (RANS) or unsteady RANS (URANS) approach with various inflow conditions;

3. development and implementation of the Lagrangian stochastic model for the prediction of the deposition of aerosol particles on the human form for various cases, and collection of the information to determine the deposition density pattern on the surface of the body.

The remainder of this report is structured as follows. The methodology to achieve the three basic steps above is discussed in detail in Section 2. In Section 3, three test cases are used to validate the proposed numerical methodology. In Section 4, the results for the detailed numerical simulations for aerosol particle deposition on the human form are reported. Finally, conclusions are given in Section 5.

Chapter 2

Numerical methods

2.1 Numerical methods for fluid flow

The time-averaged continuity equation and Reynolds-Averaged Navier Stokes (RANS) equations for an incompressible flow are given as follows:

$$\frac{\partial \overline{u}_i}{\partial x_i} = 0, \tag{2.1}$$

$$\frac{\partial \overline{u}_i}{\partial t} + \frac{\partial \overline{u}_j \overline{u}_i}{\partial x_j} = -\frac{\partial \overline{p}}{\partial x_i} + \nu \frac{\partial^2 \overline{u}_i}{\partial x_j^2} - \frac{\partial}{\partial x_j}\left(\overline{u_i^{'} u_j^{'}}\right), \tag{2.2}$$

where the Reynolds averaging of a quantity is denoted using an overbar. Summation is implied by the repeated indices. Here, $\overline{u}_i$ and $u_i^{'}$ are the mean and fluctuating (turbulent) velocities in the x_i-direction ($i = 1, 2, 3$), respectively.

Simulations using the RANS equations require less memory and computational power than other numerical methods such as direct numerical simulation (DNS) and large-eddy simulation (LES). However, all scales of the turbulence field need to be modeled (rather than simulated) in the RANS approach. Moreover, the averaging procedure in the RANS equations results in additional unknown quantities containing products of fluctuating velocities known as Reynolds stresses given as $-\overline{u_i^{'} u_j^{'}}$. In order to parametrize these Reynolds stresses, a turbulence closure model is required. The Reynolds stresses can be determined by a turbulence model, either through the turbulent viscosity hypothesis (i.e., eddy viscosity approximation) or more directly from the modeled Reynolds stress transport equations. In this study, the standard k-ε model [21] is used to parametrize the various Reynolds stresses.

The STREAM code [14] is used in this study to solve the governing equations (2.1) and (2.2) to generate the numerical fluid flow fields about the human form. STREAM is a fully-conservative, block-structured finite-volume

code for computational fluid dynamics, which employs a fully-collocated storage arrangement for all transported properties, including various turbulence quantities (e.g., turbulence kinetic energy, viscous dissipation rate, etc.). Within an arbitrary non-orthogonal coordinate system, the velocity vector is decomposed into its Cartesian components, and these are the components to which the momentum equations relate. Advective cell-face fluxes are approximated by the Upstream Monotonic Interpolation for Scalar Transport (UMIST) scheme [15], obtained by formally imposing Total Variation Diminishing (TVD) constraints on Leonard's third-order accurate Quadratic Upstream Interpolation for Convective Kinematics (QUICK) scheme [16]. A second-order fully implicit three-level scheme is used to treat the transient (or, local tendency) term. The mass continuity is enforced by solving a pressure-correction equation using the Semi-Implicit Method for Pressure-Linked Equations (SIMPLE) algorithm, which steers, as part of the iterative sequence, the pressure towards a state in which the mass residuals in all cells of the flow domain are negligibly small.

All transport equations, including the mean momentum and turbulence equations, are discretized and solved sequentially as part of the SIMPLE algorithm [17]. The linearized and discretized equations obtained in the outer iterations of the SIMPLE algorithm are solved numerically using very efficient iterative linear equation solvers, such as Stone's Strongly Implicit Procedure (SIP3D) [18] or the Conjugate Gradient Stabilized (CGSTAB) method. In conjunction with a fully-collocated approach, the SIMPLE algorithm is known to provoke checkerboard oscillations in the pressure field, reflecting a state of velocity-pressure decoupling. To avoid this, the widely used method of Rhie and Chow [19] has been adopted to interpolate the cell-face velocities from the adjacent nodal values. This interpolation essentially introduces a fourth-order "pressure smoothing" to remove the checkerboard oscillations in the pressure field. Physical diffusion fluxes are approximated using a conventional second-order accurate central differencing approach.

For mesh generation, the "ray-casting" approach [20] is used to determine whether a computational cell lies inside the complex geometry of objects encountered in the current problem, such as the human form placed within the computational domain. If the cell centroid is inside an object, the flag associated with this cell will be set to OBJECT. Otherwise, the cell flag is set to FLUID, allowing an efficient matrix solver (e.g., SIP3D) to be utilized for the solution of the discretized equations.

2.2 Particle modeling in RANS approach

Although DNS and LES have been used to study particle deposition in simple turbulent channel or pipe flows [1, 2, 7], they are still too time-consuming to be used for complex engineering problems involving particle deposition on complex surfaces. As an alternative, the unsteady Reynolds-Averaged Navier-Stokes (URANS) approach is used here for the prediction of the ensemble-averaged flow field, which is used in conjunction with eddy interaction models (EIMs, or random walk models) for the reconstruction of the instantaneous flow field. EIM is based on a Lagrangian stochastic approach where individual particles are allowed to interact successively with discrete eddies. Each eddy has length, velocity and lifetime characteristic scales obtained from the ensemble-averaged flow and turbulence fields predicted by the RANS approach. The end of the interaction between a particle and an eddy occurs when the time of interaction between the particle and eddy exceeds the lifetime of the eddy or when the particle trajectory crosses the eddy. At this instant, a new interaction of the particle with another eddy begins. The trajectory of this particular particle is obtained by solving the equations of motion for the particle [4]. In simple EIMs, the local fluctuating velocities are obtained by multiplying the root-mean-square fluid fluctuating velocity by random numbers generated from a Gaussian probability density function with zero mean and unit standard deviation at the start of an eddy-particle interaction.

Due to its simplicity, RANS(URANS)/EIM is widely used in many engineering applications, such as numerical modeling of aerosol deposition in the mouth-throat region in human upper respiratory system [5]. However, limitations associated with EIM include:

1. particles with size comparable to an eddy size cannot be accurately treated;

2. the motion of a particle does not account for the effects of neighboring particles;

3. only "one-way coupling" with the surrounding flow field is considered.

Despite such deficiencies, EIM is still an attractive tool due to its computational efficiency compared to DNS and LES, and is especially suitable for complex geometries. Therefore, URANS/EIM is selected in this study as the principal numerical methodology for predicting aerosol dispersion and deposition on the complex geometry associated with the human form under turbulent flow conditions. Details of EIM can be found in [6, 7], and its mathematical formulation is summarized briefly below.

The particle equation of motion for a sphere can be written as

$$\left(\frac{4}{3}\pi r_p^3\right)\rho_p\left(\frac{d\mathbf{u}_p}{dt}\right) = \mathbf{F}_g + \mathbf{F}_d + \mathbf{F}_B + \mathbf{F}_v + \mathbf{F}_a. \tag{2.3}$$

Here, $\mathbf{F}_g$ is the gravitational acceleration force given by

$$\mathbf{F}_g = \left(\frac{4}{3}\pi r_p^3\right)(\rho_p - \rho_f)\,\mathbf{g}; \tag{2.4}$$

$\mathbf{F}_d$ is the drag force which we parametrize using Stokes' linear resistance formulation as

$$\mathbf{F}_d = 6\pi\mu r_p\left(1 + 0.15\,\mathrm{Re}_p^{0.687}\right)(\mathbf{u}_f - \mathbf{u}_p)\,; \tag{2.5}$$

$\mathbf{F}_B$ is the Basset force given by

$$\mathbf{F}_B = 6\pi\mu r_p\int_{t_0}^{t} K\,(t-\tau)\,\frac{d\,(\mathbf{u}_f - \mathbf{u}_p)}{d\tau}d\tau; \tag{2.6}$$

$\mathbf{F}_v$ is the added mass or the inertia of the virtual mass force modeled as

$$\mathbf{F}_v = \frac{2}{3}\pi r_p^3\rho_f\frac{D\,(\mathbf{u}_f - \mathbf{u}_p)}{Dt}; \tag{2.7}$$

and, $\mathbf{F}_a$ the force caused by the fluid acceleration given by

$$\mathbf{F}_a = \frac{4}{3}\pi r_p^3\rho_f\frac{D\mathbf{u}_f}{Dt}. \tag{2.8}$$

In Eqs. (2.3)–(2.8), r_p is the radius of the spherical aerosol particle, ρ is the particle density, $\mathbf{g}$ is the gravitational acceleration, $\mathbf{u}$ is the (instantaneous) velocity, μ is the fluid viscosity, $K\,(t-\tau)$ is a kernel function, $\frac{D(\cdots)}{Dt}$ is the material derivative, and $\mathrm{Re}_p = \frac{\rho_f\left|\mathbf{u}_f - \mathbf{u}_p\right|(2r_p)}{\mu}$ is the particle Reynolds number. The subscripts f and p denote the fluid and particle phases, respectively. Except for the drag and the gravitational acceleration forces, all other terms in Eq. (2.3) are only significant when the fluid density is comparable to, or greater than, the particle density [8]. In all cases to be investigated in this report, $\rho_f/\rho_p \ll 1$ is assumed.

By reference to Figure 2.1, let us define a turbulent eddy with length scale L_e, velocity scale u_e and time scale τ_e as follows (here, the subscript "e" denotes "eddy"):

$$u_e = \sqrt{\frac{2}{3}k},\ \text{based on an isotropy assumption,} \tag{2.9}$$

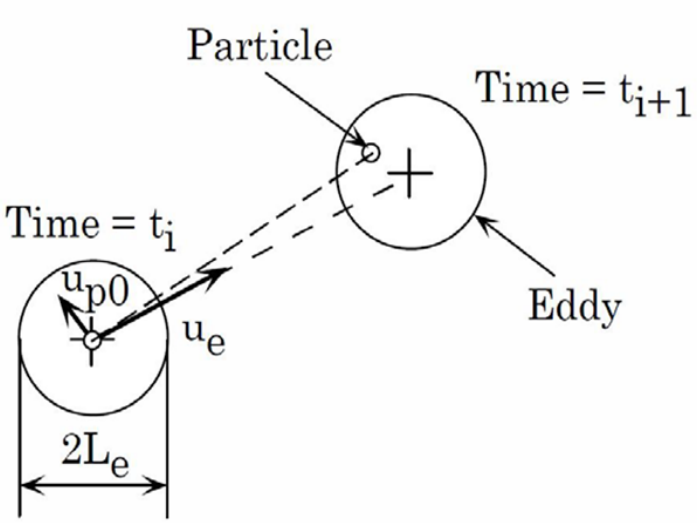

Figure 2.1: Basic concept underpinning an eddy interaction model (EIM).

$$L_e = (C_\mu)^{3/4} \frac{k^{3/2}}{\varepsilon}, \tag{2.10}$$

where L_e is the radius of a turbulent eddy depicted by a circle in Figure 2.1. From Eqs. (2.9) and (2.10), we can derive the eddy time scale (or lifetime of a turbulent eddy) as

$$\tau_e = \frac{L_e}{u_e} = \frac{(C_\mu)^{3/4} \left(k^{3/2}/\varepsilon\right)}{\sqrt{\frac{2}{3}k}}. \tag{2.11}$$

Note that k and ε in Eqs. (2.9)–(2.11) are obtained from the standard k-ε model, and $C_\mu = 0.09$ is a turbulence closure constant that defines the eddy viscosity:

$$\mu_t = C_\mu \frac{k^2}{\varepsilon}. \tag{2.12}$$

In EIM, all particles are independent of each other and there is no particle collision; viz., the classic dilute gas approximation is assumed. Any particle released from the inlet into the flow field is allowed to interact successively with various eddies, each with a radius of L_e obtained from the pre-computed turbulence (viz., k and ε) fields. This approach was referred to as "one-way coupling" earlier. The end of the interaction between a particle and an eddy occurs when the interaction time t_i exceeds the lifetime of an eddy (viz., $t_i > \tau_e$), or when the particle crosses the boundary of the eddy (i.e., when the particle is outside of the eddy depicted by a circle with a radius

of L_e in Figure 2.1). At this instant, a new interaction for the particle with another eddy is started, and the interaction time t_i is reset to zero to signal the beginning of another interaction of the particle with a new eddy. Furthermore, L_e and τ_e for the new eddy is re-calculated based on the k-ε model solutions at the particle location corresponding to the event $t_i = 0$. The particle will start to follow another trajectory through this new eddy in accordance to its equations of motion as described by Eq. (2.3) [4, 9].

As implied in Eqs. (2.3)–(2.8), the particle is driven by different forces, which are related to the instantaneous fluid velocity vector $\mathbf{u}_f \equiv \mathbf{u} \equiv \mathbf{u}_i$. However, the RANS approach only provides the mean value for this fluid velocity, namely $\overline{\mathbf{u}}_f \equiv \overline{\mathbf{u}} \equiv \overline{\mathbf{u}}_i$. Therefore, the instantaneous velocity will need to be "reconstructed" based on the mean velocity and the turbulence kinetic energy, k, as follows:

$$u_i = \overline{u}_i + u_i^{'}, \qquad i = 1, 2, 3, \tag{2.13}$$

$[(u_1, u_2, u_3) \equiv (u, v, w)]$ where the components of the fluctuating velocity are determined from

$$\begin{aligned} u^{'} &= N_u u_{rms}^{'} = N_u \sqrt{\frac{2}{3}k}, \\ v^{'} &= N_v v_{rms}^{'} = N_v \sqrt{\frac{2}{3}k}, \\ w^{'} &= N_w w_{rms}^{'} = N_w \sqrt{\frac{2}{3}k}, \end{aligned} \tag{2.14}$$

where (N_u, N_v, N_w) are random variates drawn from a Gaussian probability density function with zero mean and unit standard deviation. In order to obtain deposition density statistics, hundreds of thousands to millions of particles must be released into the flow.

Let us re-write Eq. (2.3) ignoring the Basset, virtual mass and fluid acceleration forces (owing to the fact that $\rho_f/\rho_p \ll 1$: for the cases of interest in this study):

$$\begin{aligned} \frac{d\mathbf{u}_p}{dt} &= \left(1 - \frac{\rho_f}{\rho_p}\right)\mathbf{g} + \left(\frac{6\pi\mu r_p}{\rho_p \frac{4}{3}\pi r_p^3}\right)\phi\left(\mathbf{u} - \mathbf{u}_p\right) \\ \Longrightarrow \frac{d\mathbf{u}_p}{dt} &= \left(1 - \frac{\rho_f}{\rho_p}\right)\mathbf{g} + \left(\frac{\phi}{\tau_p}\right)\left(\mathbf{u} - \mathbf{u}_p\right) \end{aligned} \tag{2.15}$$

where $\phi \equiv \left(1 + 0.15\,\mathrm{Re}_p^{0.687}\right)$ [9] and $\tau_p \equiv \left(\rho_p d_p^2\right)/\left(18\mu\right)$. Eq. (2.15) when written in component form then becomes

$$\frac{du_p}{dt} = \left(\frac{\phi}{\tau_p}\right)\left(u - u_p\right), \tag{2.16}$$

$$\frac{dv_p}{dt} = \left(\frac{\phi}{\tau_p}\right)(v - v_p)\,, \tag{2.17}$$

$$\frac{dw_p}{dt} = \left(1 - \frac{\rho_f}{\rho_p}\right) g + \left(\frac{\phi}{\tau_p}\right)(w - w_p)\,. \tag{2.18}$$

The particle equations of motion describing each particle-eddy interaction can be solved numerically by using a first-order explicit time stepping scheme:

$$\frac{d\mathbf{u}_p}{dt} \simeq \frac{\mathbf{u}_p^{n+1} - \mathbf{u}_p^n}{\Delta t} = \left(1 - \frac{\rho_f}{\rho_p}\right)\mathbf{g} + \left(\frac{\phi}{\tau_p}\right)(\mathbf{u} - \mathbf{u}_p) \Longrightarrow \text{find } \mathbf{u}_p^{n+1}; \tag{2.19}$$

$$\frac{\mathbf{x}_p^{n+1} - \mathbf{x}_p^n}{\Delta t} = \mathbf{u}_p^{n+1} \Longrightarrow \text{find } \mathbf{x}_p^{n+1}. \tag{2.20}$$

This numerical scheme is applied to determine the trajectory for each particle released into the flow. The particle interacts with a sequence of random eddies representing the instantaneous flow (or, velocity) field, and the trajectory of this particle is tracked until it collides with a solid surface (e.g., the ground surface, the surface representing the human body, etc.) or exits from the boundaries of the computational domain. The time step that is used in Eqs. (2.19)–(2.20) is an adaptive time step and reset at the start of each eddy-particle interaction as the particle enters a new eddy. The time step is chosen to be the minimum of one fifth of the eddy lifetime or one fifth of the minimum side length of the local element, $L_{\min}$, divided by the particle local velocity [10]; viz.,

$$\Delta t = \min\left(\frac{\tau_e}{5}, \left(\frac{1}{5}\right)\frac{L_{\min}}{\sqrt{u_p^2 + v_p^2 + w_p^2}}\right). \tag{2.21}$$

Upon a particle-solid surface impaction (i.e., a particles is assumed to deposit and stick to a solid surface when the centroid location of the particle reaches a distance from the surface equal to the radius of the particle or less), the particle position is recorded and the particle is assumed to be permanently removed from the flow. In other words, a "sticky wall" condition is imposed so that no rebounding or resuspension of a particle from a surface is considered in the modeling. By counting the number of particles entering and leaving the sample section, the deposition density distribution can be obtained. Near a solid surface, the eddy lifetime is assumed to be a constant and equal to the minimum Lagrangian time scale [11]. This approach is efficient in circumventing the problem that occurs near walls (and other solid surfaces), where the eddy lifetimes could tend to vanishingly small values, which will increase significantly the overall computational time.

Chapter 3

Numerical validation

In order to validate the implementation of EIM and assess the performance of using the k-ε model for provision of the flow field to drive the dispersion of the aerosol particles, we consider a two-phase turbulent impinging jet, which was investigated experimentally in [12] and numerically in [10]. A schematic of the computational domain from [12] is given in Figure 3.1 for illustrative purposes.

To be consistent with the experiment of [12], incompressible and steady state fluid flow at a standard temperature and pressure (STP) will be assumed for the simulations. The inlet conditions consist of a constant inlet velocity $U_j = 10.5$ m s^{-1}, a turbulence intensity of 5% of the mean velocity and a turbulence length scale of 10% of the inlet diameter. The Reynolds number based on the inlet diameter is

$$\mathrm{Re} = \frac{\rho U_j D}{\mu} = \frac{(1.18)\,(10.5)\,(0.015)}{1.824 \times 10^{-5}} = 10189 \simeq 10^4. \tag{3.1}$$

The standard no slip boundary condition (BC) will be applied to the walls and a zero gauge pressure BC or a zero gradient (Neumann) BC combined with bulk mass flow correction will be used at the outlet of the computational domain.

The particle Stokes number is defined as

$$Stk = C_c \frac{\rho_p U_j d_p^2}{9\mu D} \simeq (1) \frac{(1050)\,(10.5)\,(5 \times 10^{-6})^2}{(9)\,(1.824 \times 10^{-5})\,(0.015)} = 0.112, \tag{3.2}$$

where $C_c \simeq 1$ is the Cunningham slip factor, $\rho_p = 1050$ kg m^{-3} is the particle density, and $d_p = 5$ μm is the particle diameter. Experimental data are available for $L/D = 2$, 4 and 6 9 (see Figure 3.1).

Because the computational domain is axi-symmetric, we use a two-dimensional axi-symmetric code to solve the governing equations for the fluid flow.

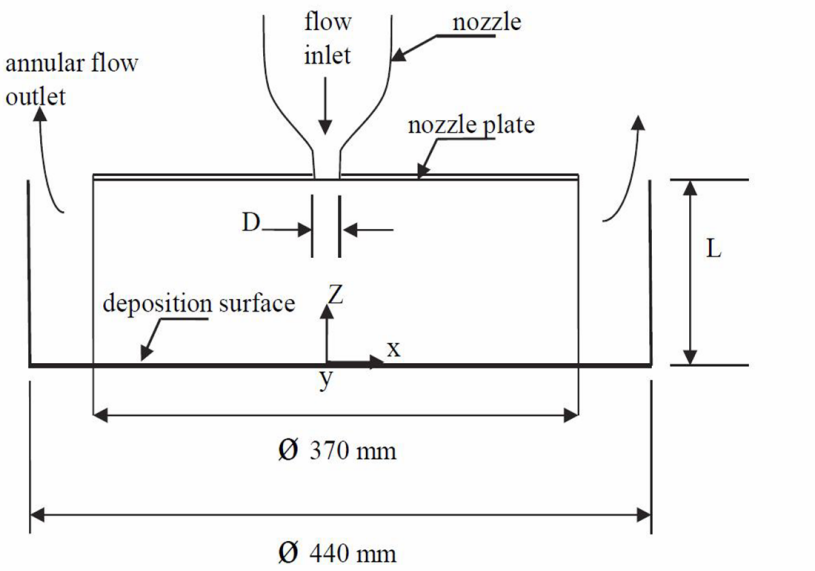

Figure 3.1: A schematic of the computational domain for the two-phase impinging jet based on the experimental study conducted in [12].

A total of $10,000$ particles were released into the computational domain. The initial velocity of each particle was set equal to the fluid velocity. The particles were randomly and uniformly distributed in space at the inlet. Two types of particle tracking were tested: namely, "turbulent tracking" and "mean flow tracking". In turbulent tracking, the instantaneous velocity of the flow in the particle equations of motion is taken to be the sum of the mean and fluctuating flow velocities. In mean flow tracking, the instantaneous velocity of the flow is simply taken to be equal to the mean flow velocity (viz., the fluctuating flow velocity is assumed to be zero).

The particle deposition density profiles, using turbulent tracking (i.e., turbulent dispersion) and mean flow tracking (i.e., without turbulent dispersion) versus the radial distance from the stagnation point, r/D, are shown in Figures 3.2, 3.3 and 3.4 for $L/D = 2$, 4 and 6, respectively. These particle simulations were performed using EIM. The experimental data of Burwash et al. [12] for $L/D = 2$, 4 and 6 are shown for comparison. Table 3.1 shows the deposition efficiency defined as the percentage of the number of particles deposited on the wall for the three cases. The experimental results and numerical results from CFX 5.7.1 [12] are summarized in the table as well. A perusal of Figures 3.2, 3.3 and 3.4 and of Table 3.1 shows that the turbulent tracking tends to overpredict the deposition density when compared to the

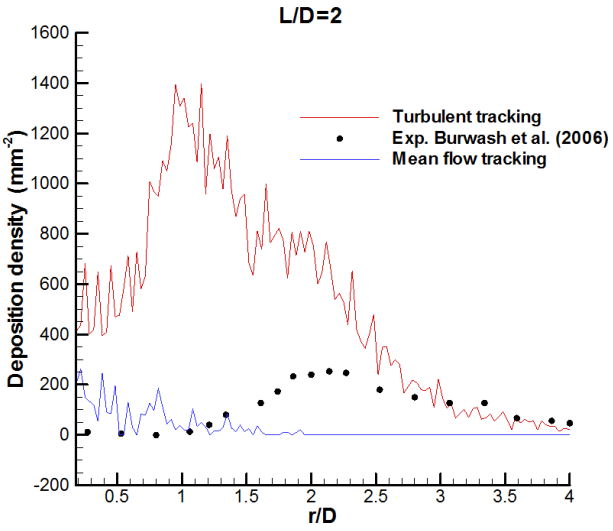

Figure 3.2: Deposition density obtained with turbulent tracking and mean flow tracking for $L/D = 2$ using the classical EIM.

experimental measurements for $L/D = 2$, 4 and 6. This overprediction is not unexpected because of the isotropy assumption employed in the k-ε turbulence model. The isotropy assumption gives larger turbulence intensities (i.e., excessive turbulence kinetic energy) than the actual component normal to the wall, which plays an important role for particle deposition, and thus causes more deposition. From the figures, it can be deduced that the accurate modeling of the near-wall effects on turbulence features is important for the prediction of the deposition rates.

In contrast to the turbulent tracking, the mean flow tracking, where the particles are deposited by the means of the inertial impaction mechanism, underpredicts the deposition density, when compared to the experimental measurements. The underprediction (for $L/D = 2$, 4 and 6) of the deposition density is expected because at a size of 5 μm, most of the particles owing to their small inertia, will tend to follow the mean flow field and only a few of them will deposit on the impingement wall. These results therefore suggest that the turbulent dispersion mechanism which drives the turbulent tracking is the main mechanism that causes the particles to deposit on the impingement wall.

In a turbulent flow, the turbulent dispersion (i.e., by the fluid flow fluctuations) is the main mechanism for particle deposition, especially for small

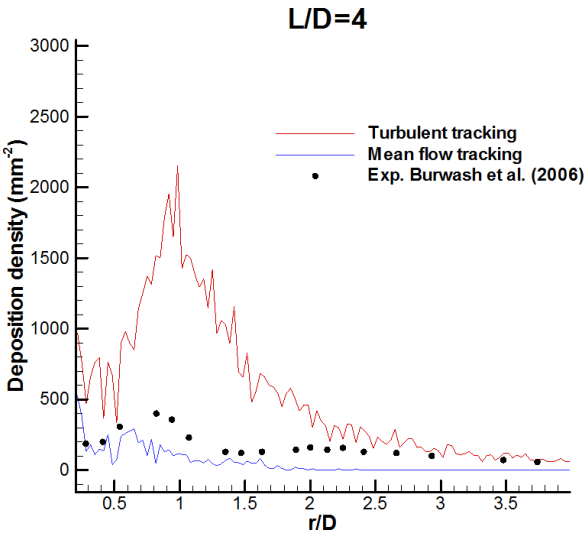

Figure 3.3: Deposition density obtained with turbulent tracking and mean flow tracking for $L/D = 4$ using the classical EIM.

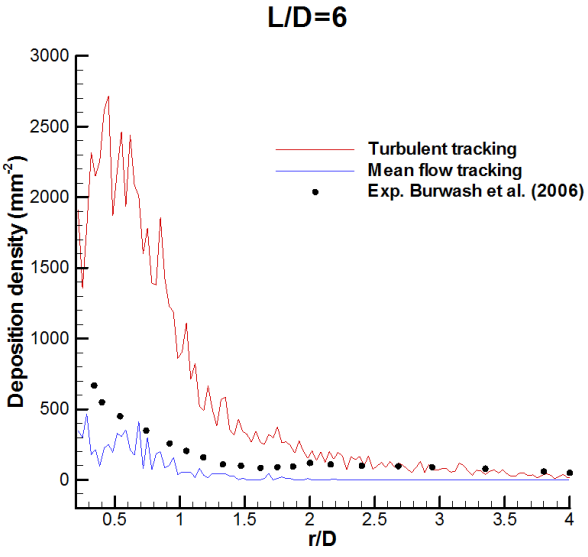

Figure 3.4: Deposition density obtained with turbulent tracking and mean flow tracking for $L/D = 6$ using classical EIM.

L/D	Turbulent tracking	Mean flow tracking	CFX 5.7.1	Exp. Burwash (2006)
2	56%	1.4%	75%	16.5%
4	57%	2.9%	77.4%	17%
6	41%	2.3%	82%	17.8%

Table 3.1: Comparison of the deposition efficiency obtained from turbulent tracking and mean flow tracking with experimental measurements.

particle sizes (5 μm and Stk = 0.11). Therefore, the appropriate modeling of the fluid fluctuations in the near-wall region is crucial for accurate simulations of the particle deposition on a surface. It is known that, the k-ε turbulence model is formulated implicitly with an isotropic decomposition of the turbulence kinetic energy ($u_{rms}^{'} = v_{rms}^{'} = w_{rms}^{'} = (2k/3)^{1/2}$). The use of $(2k/3)^{1/2}$ for the velocity standard deviation for all components results in an overprediction of the normal-to-wall fluctuating velocity component, which is the main component responsible for particle deposition on the impingement wall, near the stagnation point and in the wall jet region. As a result, the overprediction of the normal-to-wall fluctuating velocity will cause an overprediction in the deposition as was shown in Figures 3.2, 3.3 and 3.4.

For this reason, some improvements are needed to account for the near-wall features in the near-wall region. Therefore, to improve the prediction of the particle deposition, a near-wall correction [13] is used in this study. With the near-wall correction, the fluctuating velocity in the wall normal direction near a wall can be written as:

$$\begin{aligned} u^{'} &= f_u N_u u_{rms}^{'} = N_u \sqrt{\frac{2}{3}k}, \\ f_u &= 1 - e^{-0.02y^+}, \quad y^+ < 80 \end{aligned} \tag{3.3}$$

where the dimensionless wall distance y^+ is calculated using the formula $y^+ = yu^*/\nu$, and $u^* = \sqrt{\tau_w/\rho}$. Here, τ_w is the wall shear stress, and y is the normal distance to the impingement wall.

Figures 3.5, 3.6 and 3.7 show the deposition density curves as a function of r/D for $L/D = 2$, 4 and 6 obtained with turbulent tracking and the near-wall correction. Table 3.2 shows the deposition efficiency for the three cases obtained with turbulent tracking and a near-wall correction. As evident in Figures 3.5–3.7 and in Table 3.2, application of turbulent tracking with a near-wall correction yielded much better results than that without a near-wall correction when compared to the experimental measurements [12].

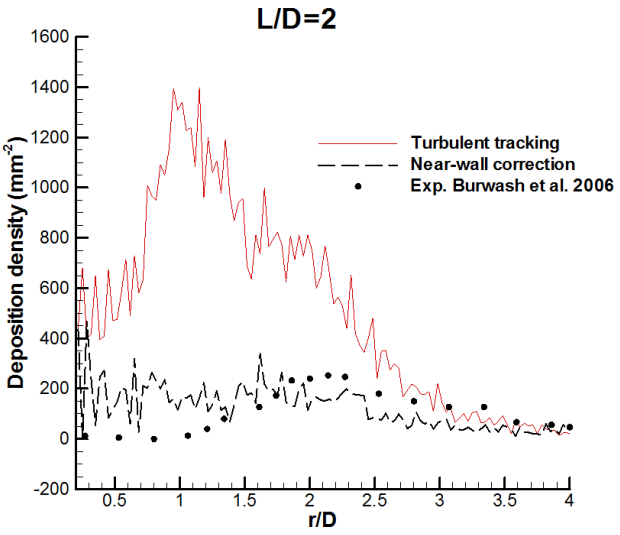

Figure 3.5: Deposition density for $L/D = 2$ obtained from turbulent tracking and a near-wall correction.

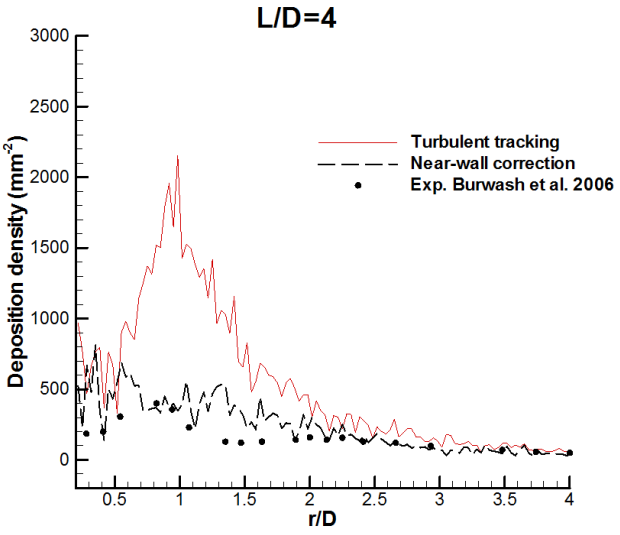

Figure 3.6: Deposition density for $L/D = 4$ obtained from turbulent tracking and a near-wall correction.

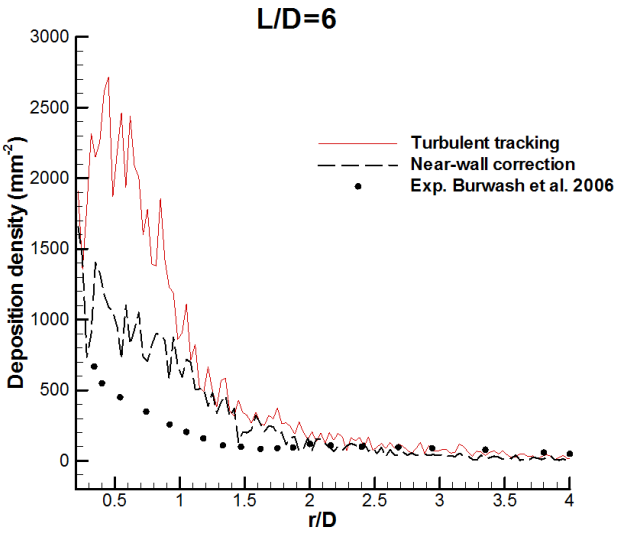

Figure 3.7: Deposition density for $L/D = 6$ obtained from turbulent tracking and a near-wall correction.

L/D	Turbulent tracking	Near-wall correction	CFX 5.7.1	Exp. Burwash (2006)
2	56%	32%	75%	16.5%
4	57%	27%	77.4%	17%
6	41%	25%	82%	17.8%

Table 3.2: The deposition efficiency obtained from turbulent tracking with and a without a near-wall correction in comparison with some experimental measurements.

Chapter 4

Aerosol particle deposition on the human form

4.1 Numerical parameters

A full-size 1.8 meter tall human form in the standing position is shown in Figure 4.1. The non-dimensional computational domain size based on the human height (as the reference length) are $[-2, 8]$ in x-direction (or, streamwise direction), $[-2, 2]$ in y-direction (or, spanwise direction) and $[-0.5, 2]$ in z-direction (or, vertical direction). The human form is positioned at $(0, 0, -0.5)$ in the computational domain as illustrated in Figure 4.2. The human face is oriented at three orientations (viz., 0, 90, and 180 degrees) with respect to the incident wind direction which is assumed to be along the $+x$ direction. These three orientations of the human form with respect to the incident wind direction are shown in Figure 4.3 (a), (b) and (c), which correspond, respectively, to 0 degree (human facing the wind), 90 degrees (human facing direction 90 degree from the incident wind direction), and 180 degrees (human facing away from the wind).

The uniform inlet wind velocity at the $x = -2$ plane is 2.5 m s^{-1}. The Reynolds number based on the inlet wind velocity and height of the human form is

$$\mathrm{Re} = \frac{\rho U H}{\mu} = \frac{(1.18)\,(2.5)\,(1.8)}{(1.824 \times 10^{-5})} = 2.91 \times 10^5. \tag{4.1}$$

The standard no slip boundary condition (BC) is applied to the walls (and body surface of the human form) and a zero gradient (Neumann) BC combined with a bulk mass flow correction is used at the outlet of the computational domain. The simulation is carried out in a three-dimensional Cartesian framework, and the curved surfaces on the human form that are not aligned

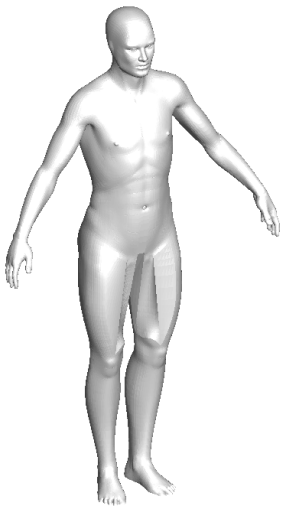

Figure 4.1: A model of the human form used for the simulation of aerosol particle deposition.

with the grid lines are approximated by stepwise surfaces. A mesh consisting of $100 \times 70 \times 70$ grid lines in the x-, y-, and z-directions, respectively, is used to accommodate all the necessary geometrical details. The grid arrangement adopted here is shown in Figure 4.4. The grid lines are preferentially concentrated near the human body surfaces (and other solid surfaces) where the gradients in the flow properties are expected to be greatest, and the spacing between the grid lines is gently stretched with increasing distance from the solid surfaces.

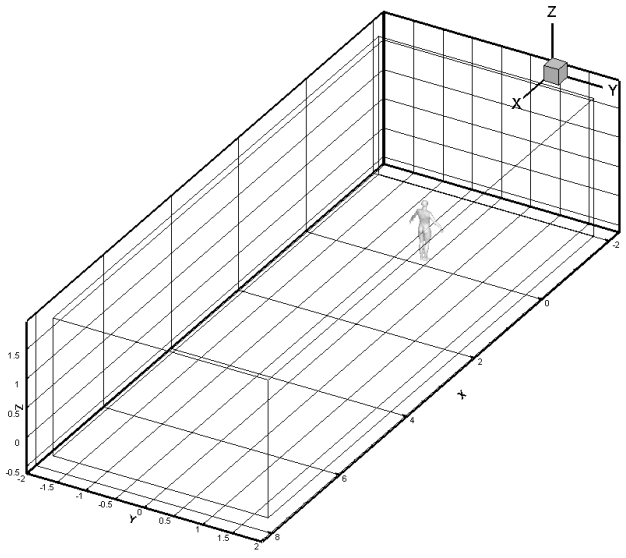

Figure 4.2: The non-dimensional computational domain used for the simulation of the aerosol particle deposition on a human form.

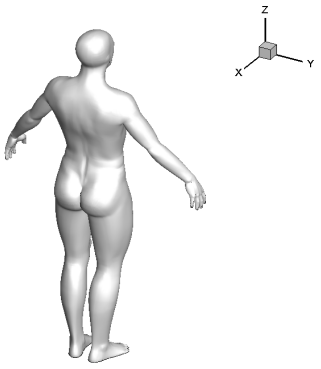

(a)

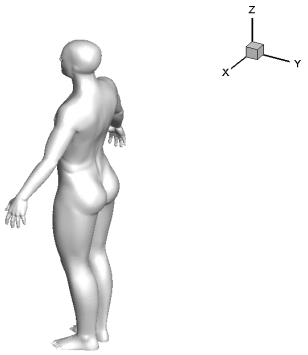

(b)

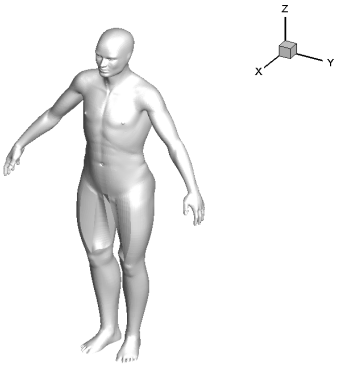

(c)

Figure 4.3: The human form is directed at three different orientations with respect to the incident wind direction: (a) 0, (b) 90, and (c) 180 degrees corresponding to a human form facing into, facing 90 degrees from, and facing away from the direction of the incoming wind, respectively.

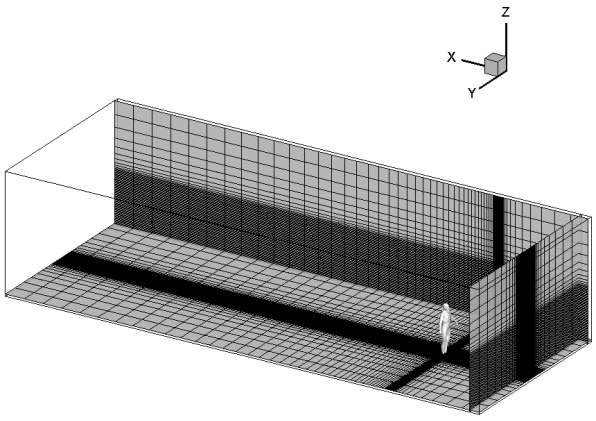

Figure 4.4: Generated three-dimensional computational grid.

4.2 Flow fields

The generated turbulent flow fields about the human form for the three cases, corresponding to the human form oriented at 0, 90 and 180 degrees with respect to the incoming wind direction, are summarized in Figures 4.5–4.10. For visualization purposes, the flow fields and streamlines at two cross sections through the human form are exhibited: namely, in a vertical x-z plane bisecting the human form along a vertical axis and in a horizontal x-y plane bisecting the human form at half height. From these figures, it can seen that complicated vortices and swirling flow are generated around and behind the human form.

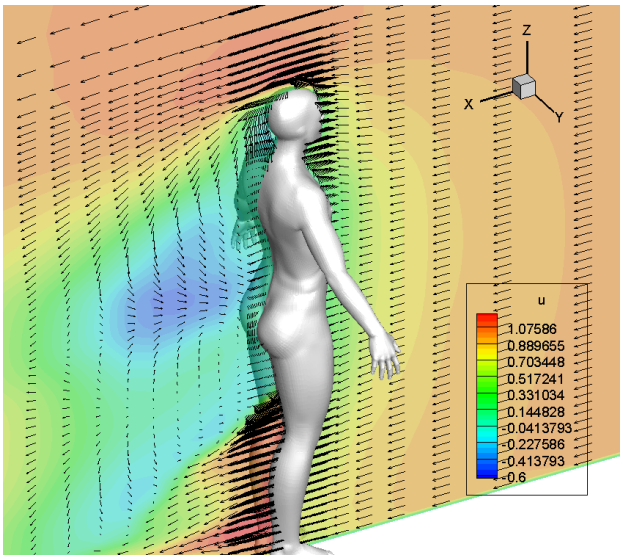

(a)

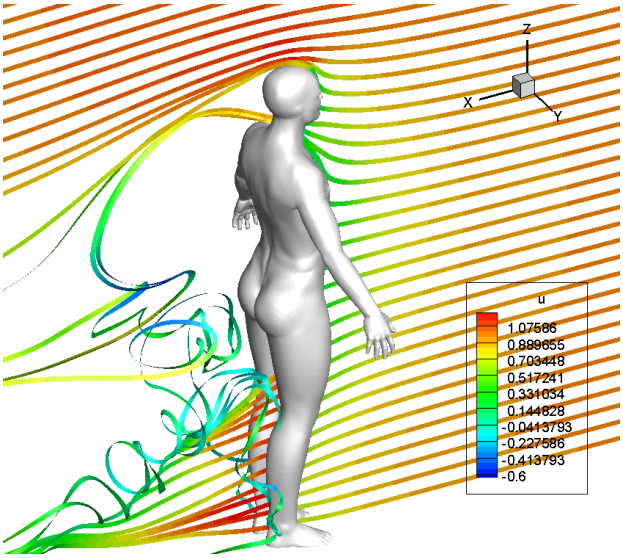

(b)

Figure 4.5: Flow field (a) and streamlines (b) in a vertical x-z plane of the computational domain bisecting the human form for the case of a 0 degree orientation relative to the incident wind direction.

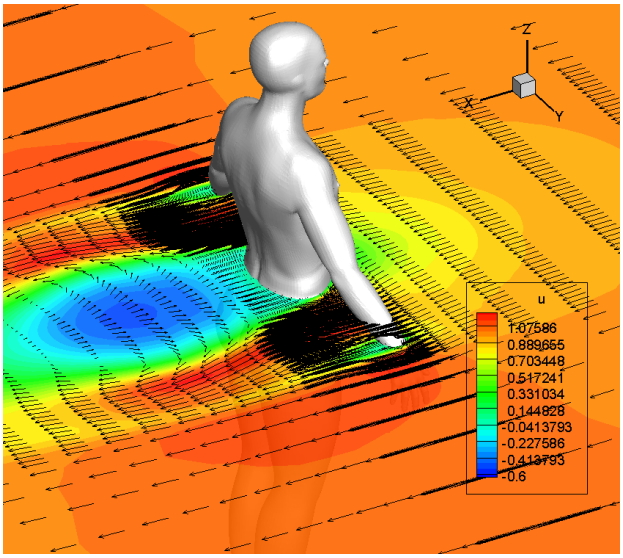

(a)

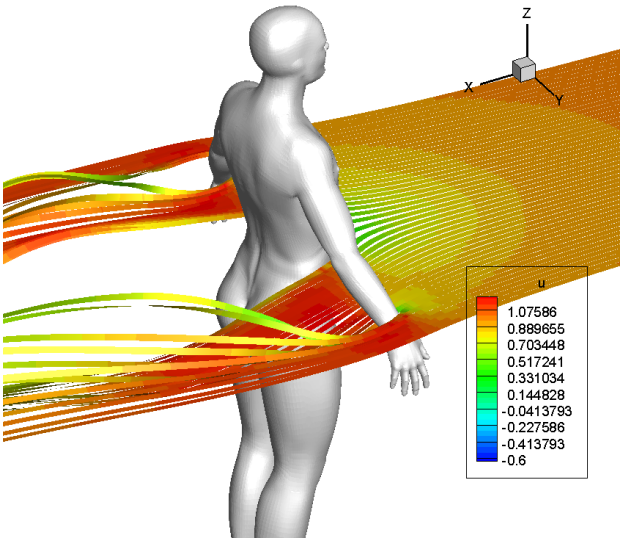

(b)

Figure 4.6: Flow field (a) and streamlines (b) in a horizontal x-y plane of the computational domain bisecting the human form at half height for the case of a 0 degree orientation relative to the incident wind direction.

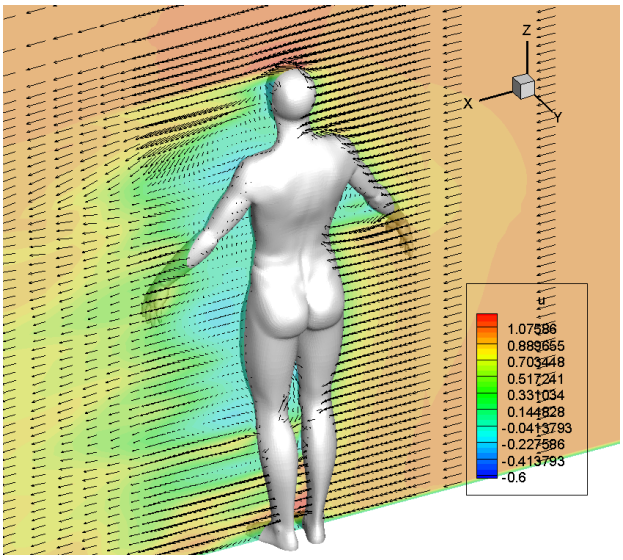

(a)

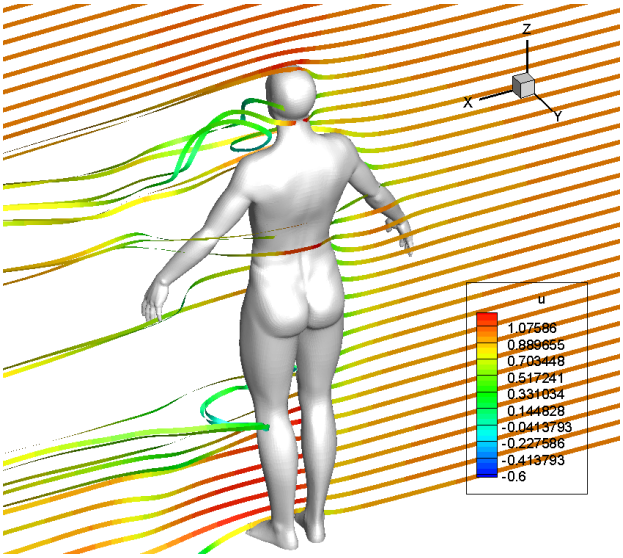

(b)

Figure 4.7: Flow field (a) and streamlines (b) in a vertical x-z plane of the computational domain bisecting the human form for the case of a 90 degree orientation relative to the incident wind direction.

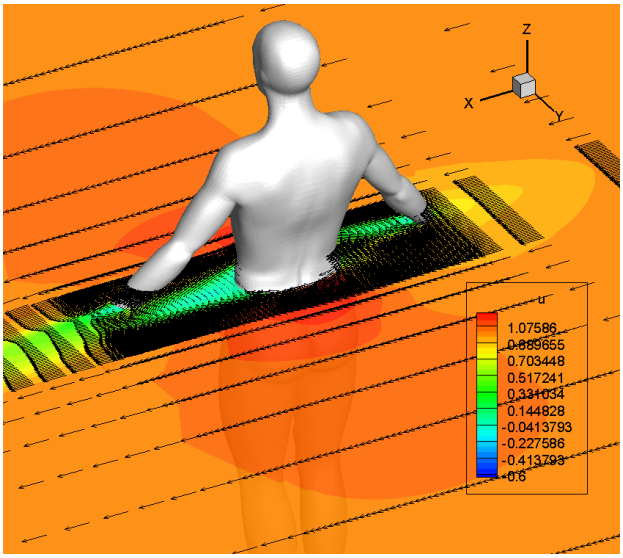

(a)

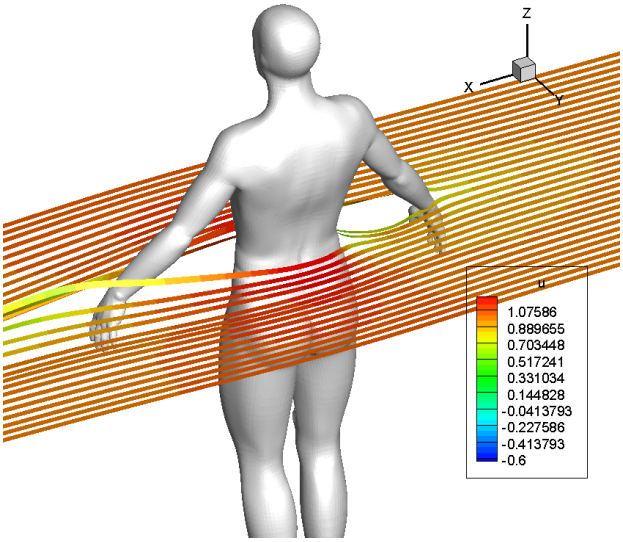

(b)

Figure 4.8: Flow field (a) and streamlines (b) in a horizontal x-y plane of the computational domain bisecting the human form at half height for the case of a 90 degree orientation relative to the incident wind direction.

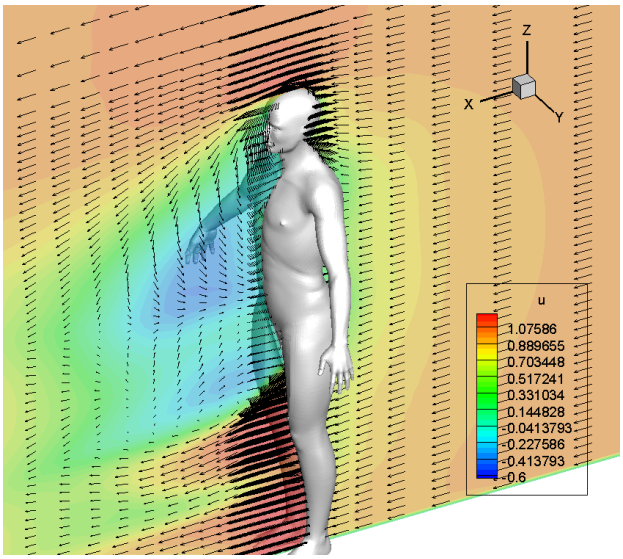

(a)

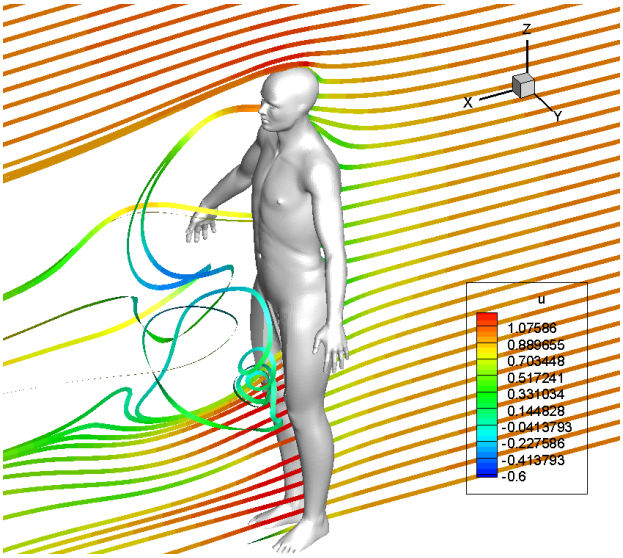

(b)

Figure 4.9: Flow field (a) and streamlines (b) in a vertical x-z plane of the computational domain bisecting the human form for the case of a 180 degree orientation relative to the incident wind direction.

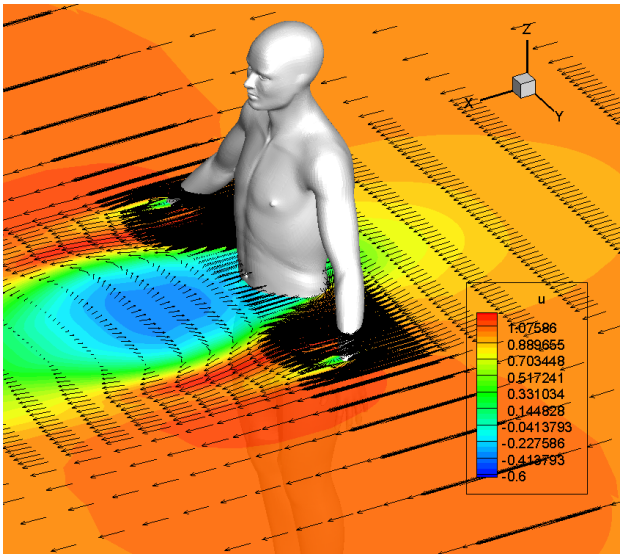

(a)

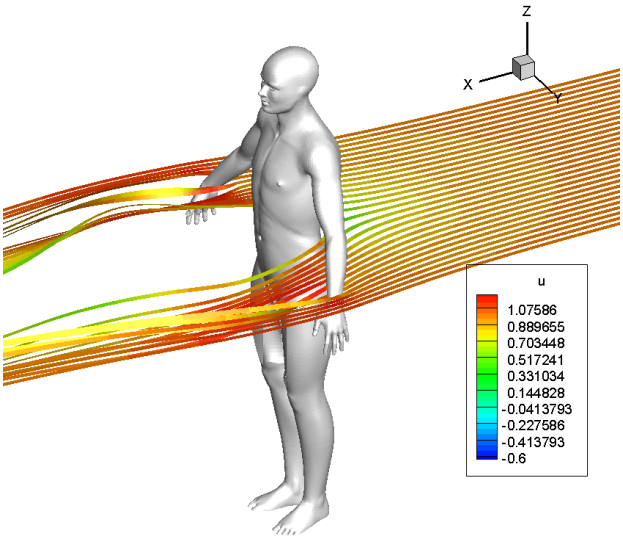

(b)

Figure 4.10: Flow field (a) and streamlines (b) in a horizontal x-y plane of the computational domain bisecting the human form at half height for the case of a 180 degree orientation relative to the incident wind direction.

4.3 Aerosol particle deposition

In this study, we used thirteen different diameters of aerosol particles in our simulation: namely, 0.1585, 0.2511, 0.3981, 0.631, 1.0, 1.585, 2.511, 3.981, 6.31, 10.0, 15.85, 25.118 and 39.812 μ. The particle density is 1008 kg m^{-3}. For each particle size, one million particles located with a uniform random distribution on the inlet plane is released (at $x = -2$) into the non-dimensionalized computational domain. The mesh representing the body surface of the human form consists of 178,716 triangular cell which tessellate the entire body surface. The number of particles that impact a triangular cell of this surface mesh are counted in each simulation. The deposition density on each triangular cell is defined as to be the product of the mass of each particle and the number of particles that deposit in the cell divided by the area of the triangular cell with units of g m^{-2}. From this information, the deposition probability in each triangular cell is obtained by dividing the deposition density in the cell by the challenge particle mass per unit area on the inlet plane (recall that the areal particle mass density on the inlet plane is uniform).

The isopleths of the deposition probability for each particle size and for each orientation of the human form at that particle size are exhibited in Figures 4.11–4.49. In each of these figures, the human form is displayed in four views: namely, front view, rear view, right side view, and left side view.

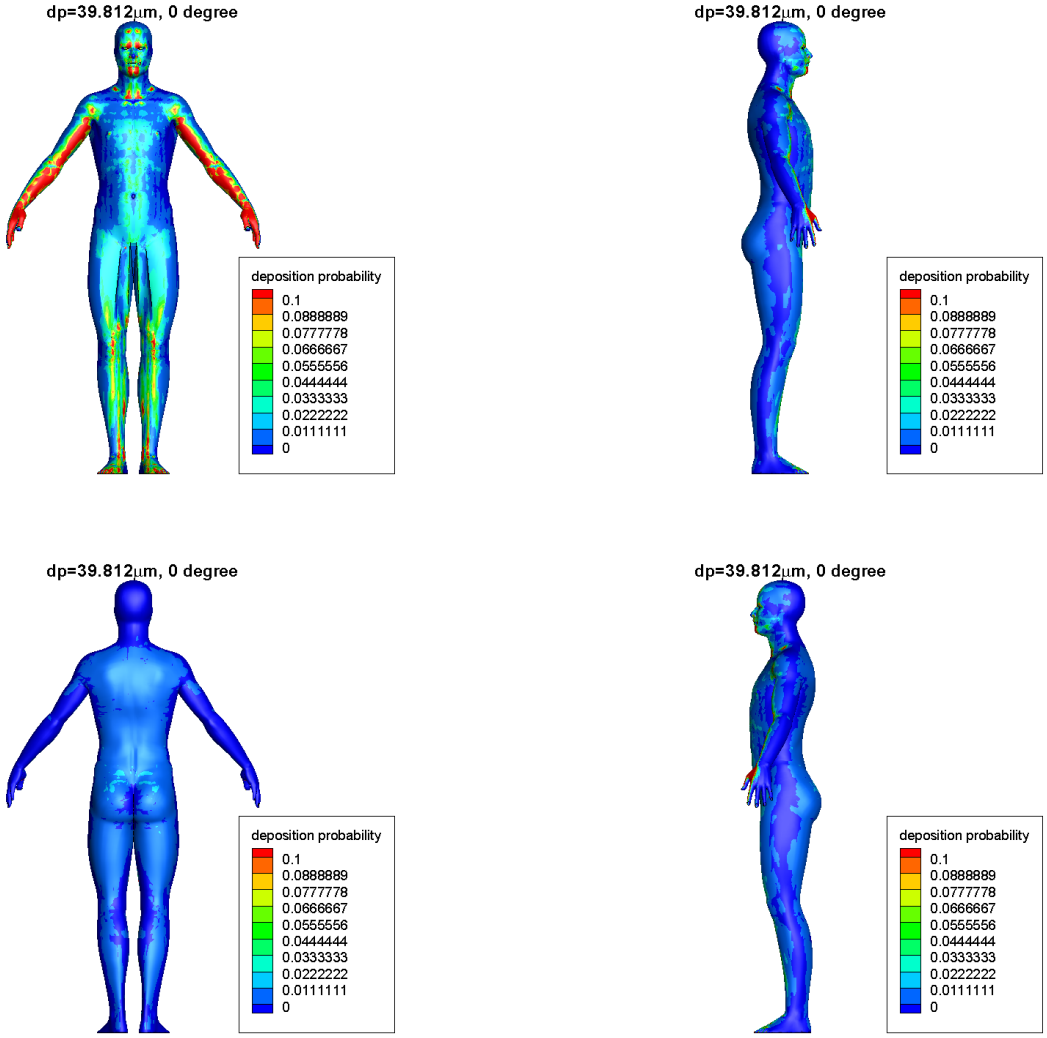

Figure 4.11: Isopleths of the deposition probability for a particle diameter of $d_p = 39.812$ μm for the human form oriented at 0 degree with respect to the incident wind direction.

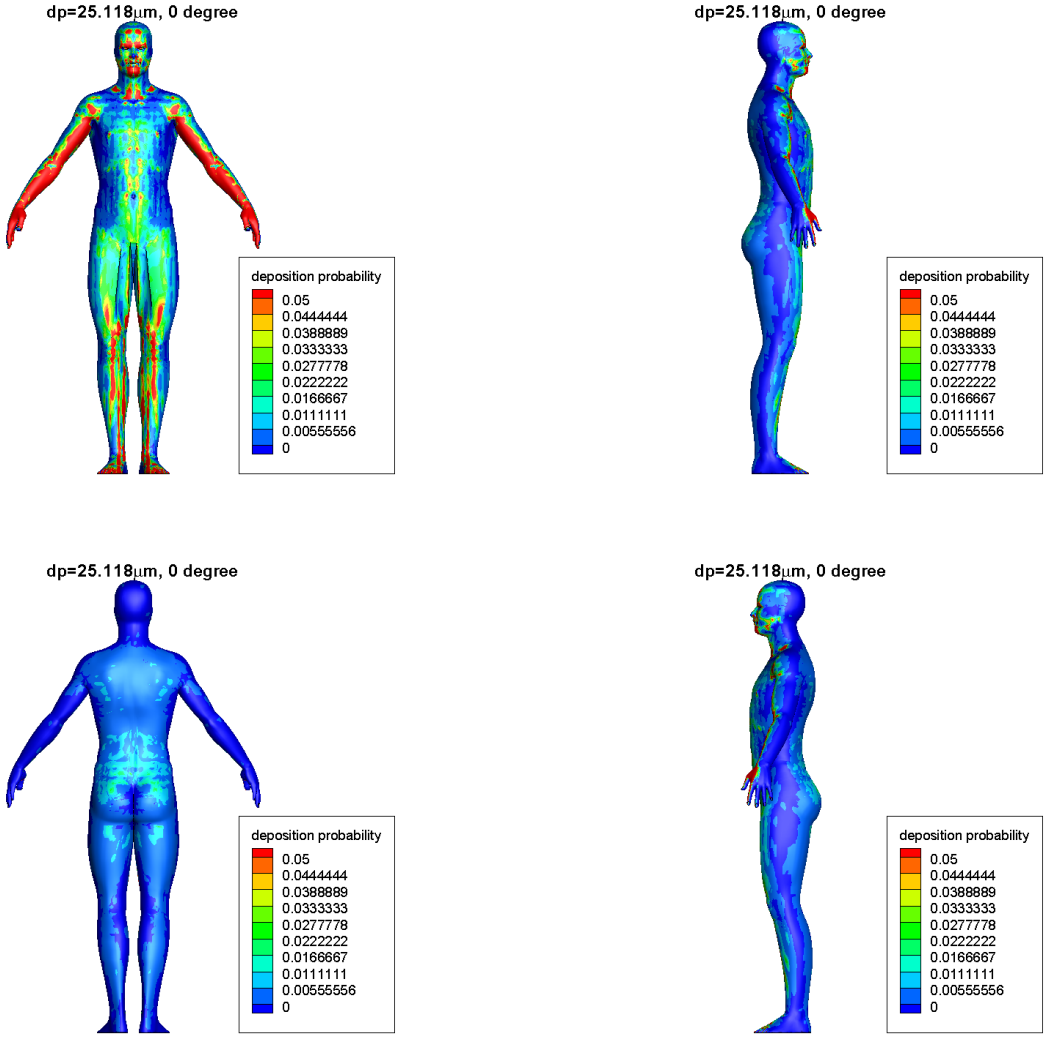

Figure 4.12: Isopleths of the deposition probability for a particle diameter of $d_p = 25.118$ μm for the human form oriented at 0 degree with respect to the incident wind direction.

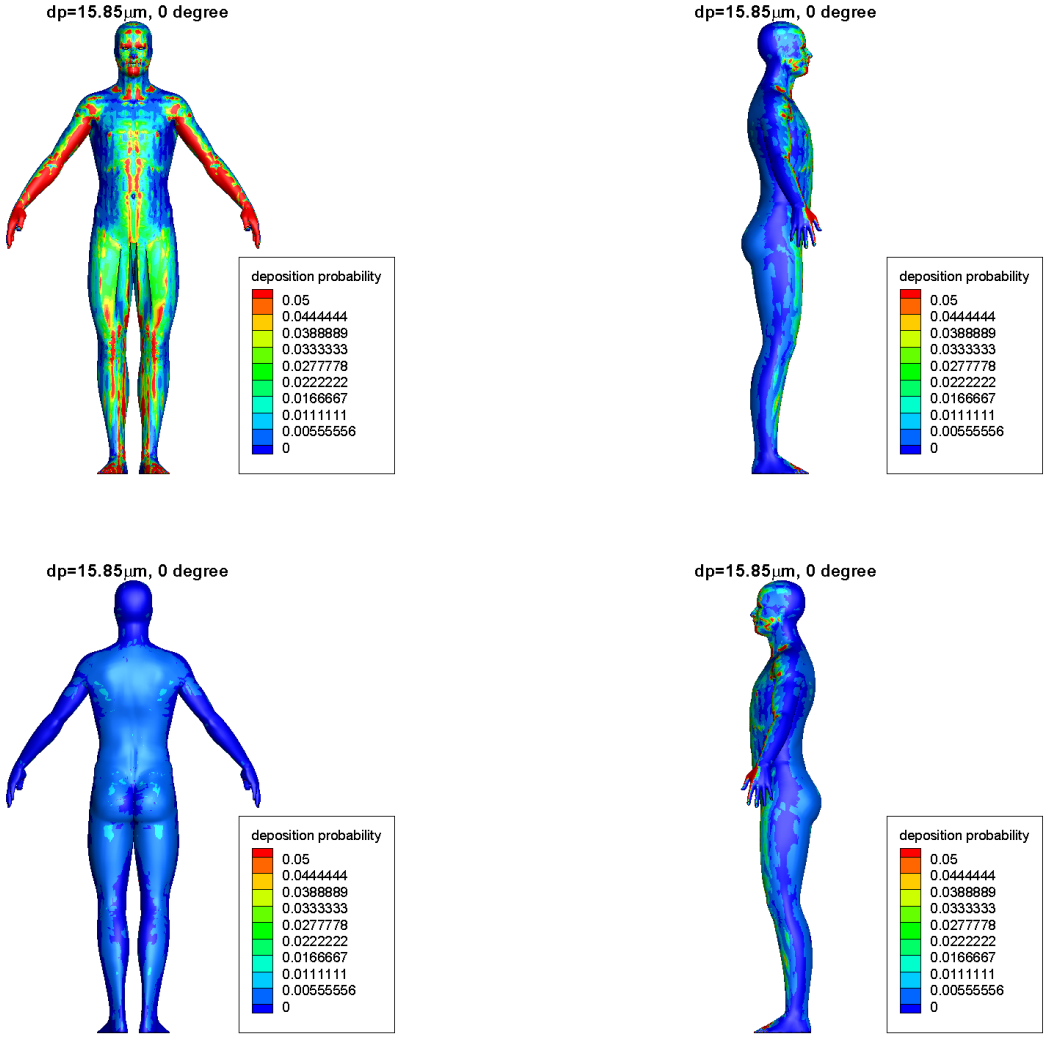

Figure 4.13: Isopleths of the deposition probability for a particle diameter of $d_p = 15.85$ μm for the human form oriented at 0 degree with respect to the incident wind direction.

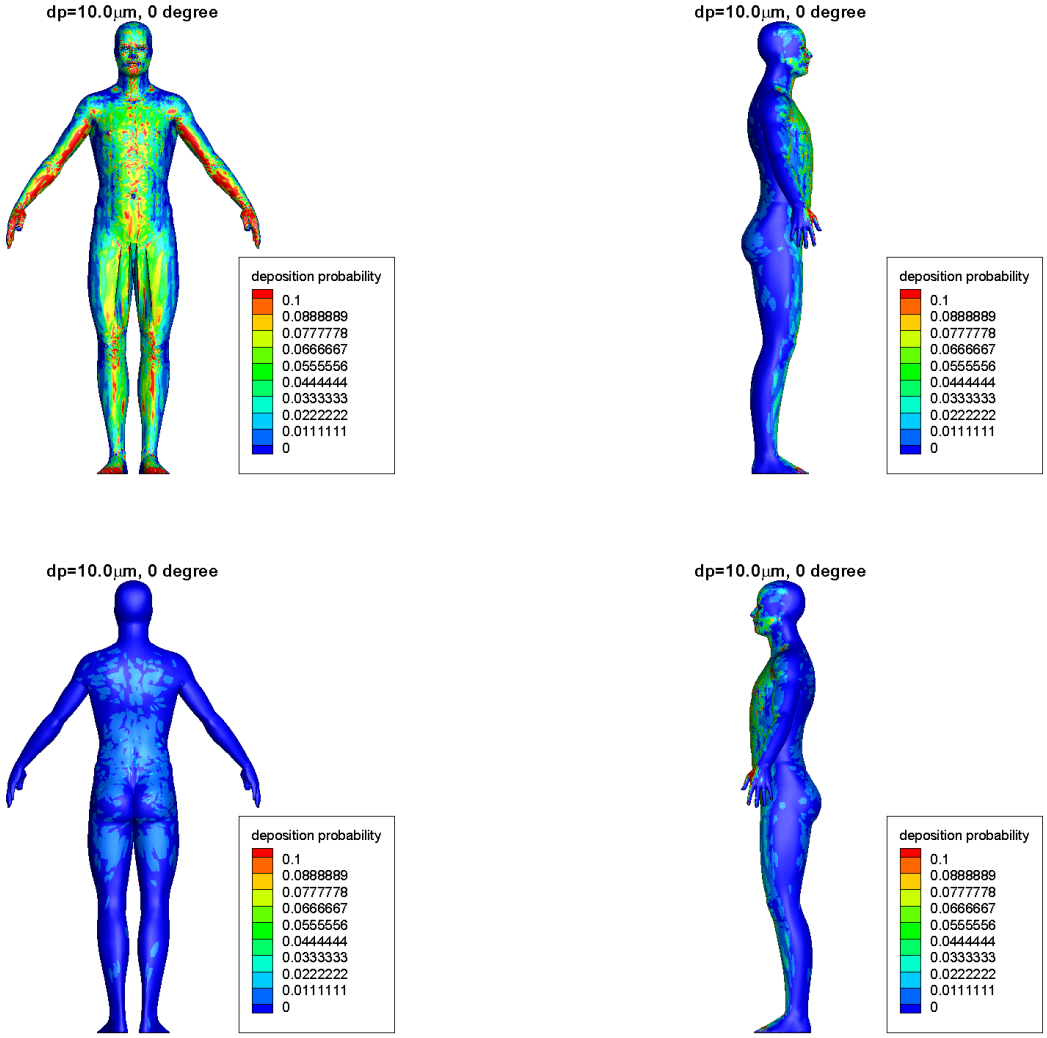

Figure 4.14: Isopleths of the deposition probability for a particle diameter of $d_p = 10.0$ μm for the human form oriented at 0 degree with respect to the incident wind direction.

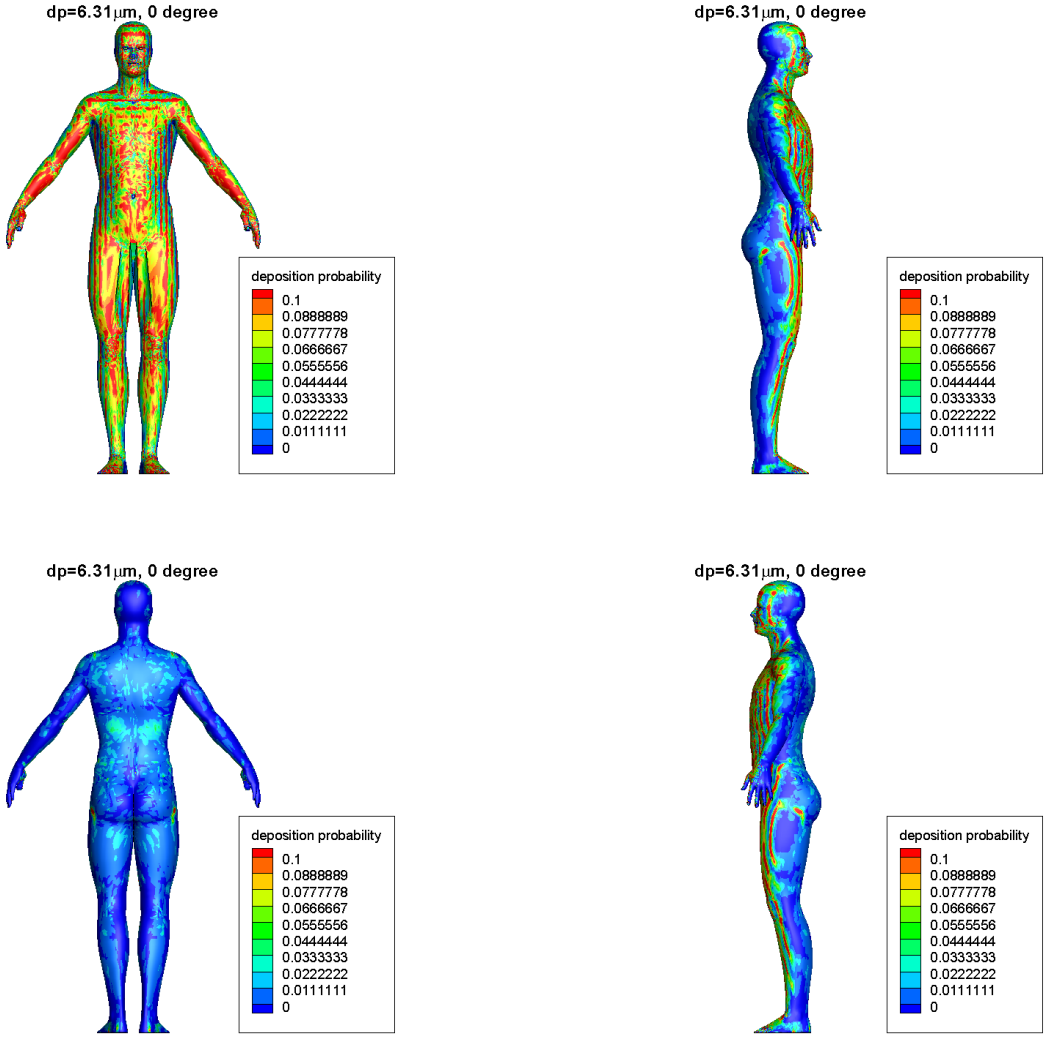

Figure 4.15: Isopleths of the deposition probability for a particle diameter of $d_p = 6.31$ μm for the human form oriented at 0 degree with respect to the incident wind direction.

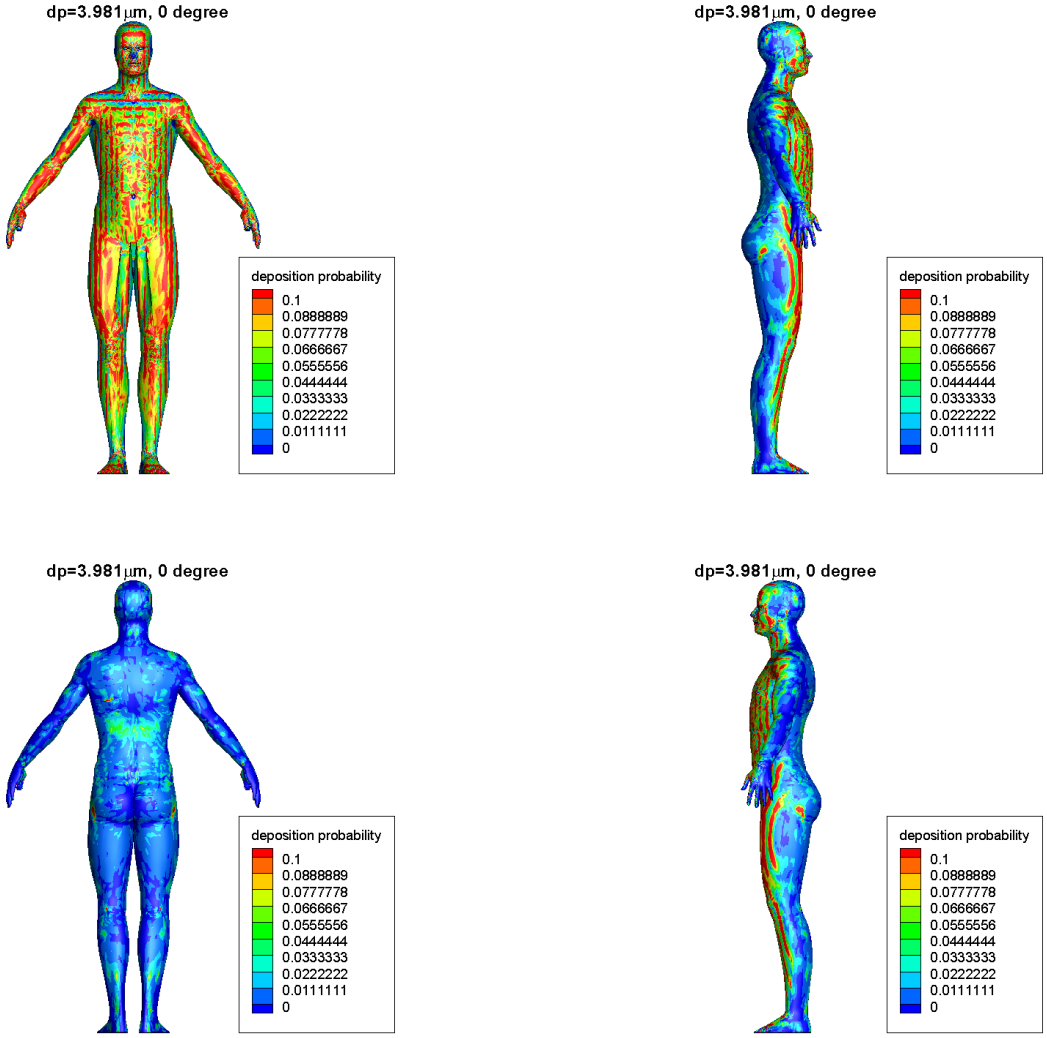

Figure 4.16: Isopleths of the deposition probability for a particle diameter of $d_p = 3.981$ μm for the human form oriented at 0 degree with respect to the incident wind direction.

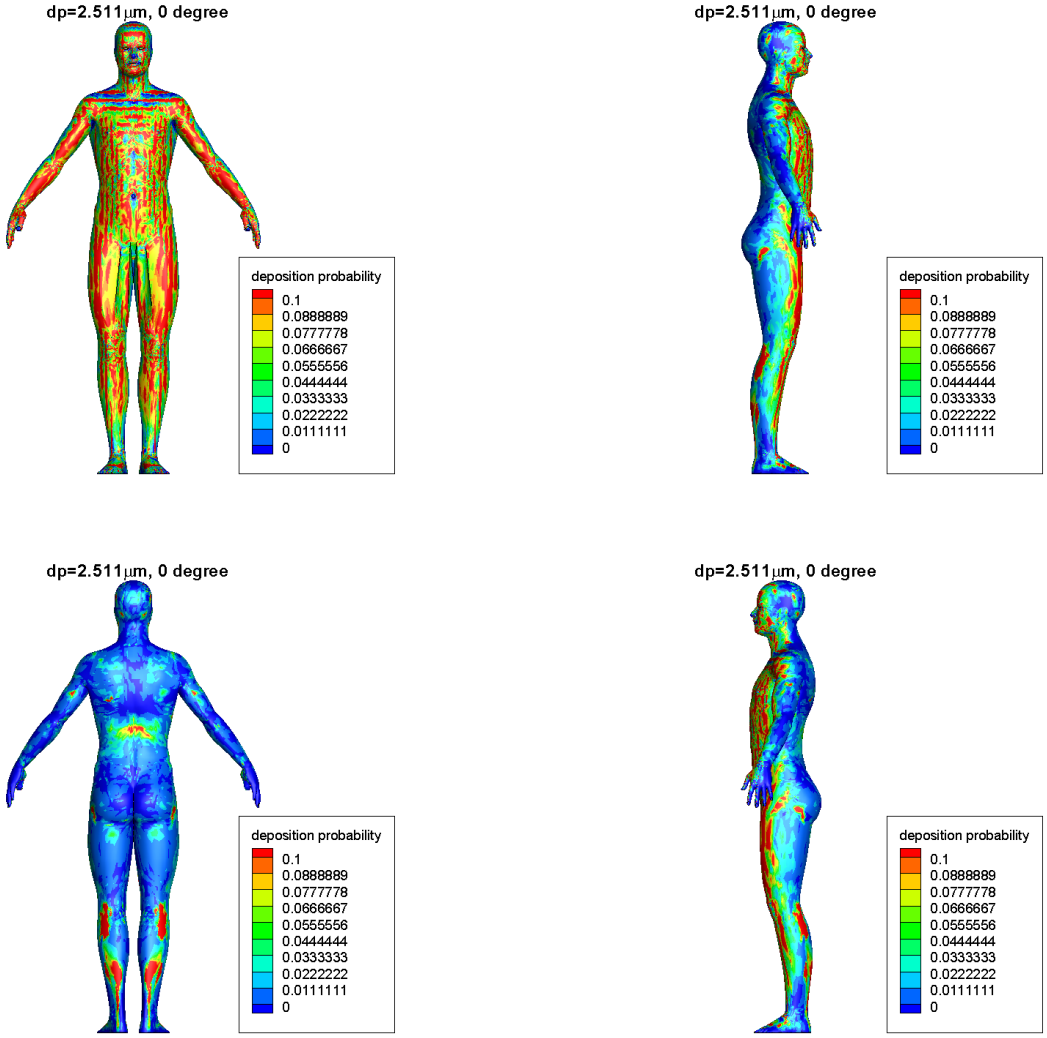

Figure 4.17: Isopleths of the deposition probability for a particle diameter of $d_p = 2.511$ μm for the human form oriented at 0 degree with respect to the incident wind direction.

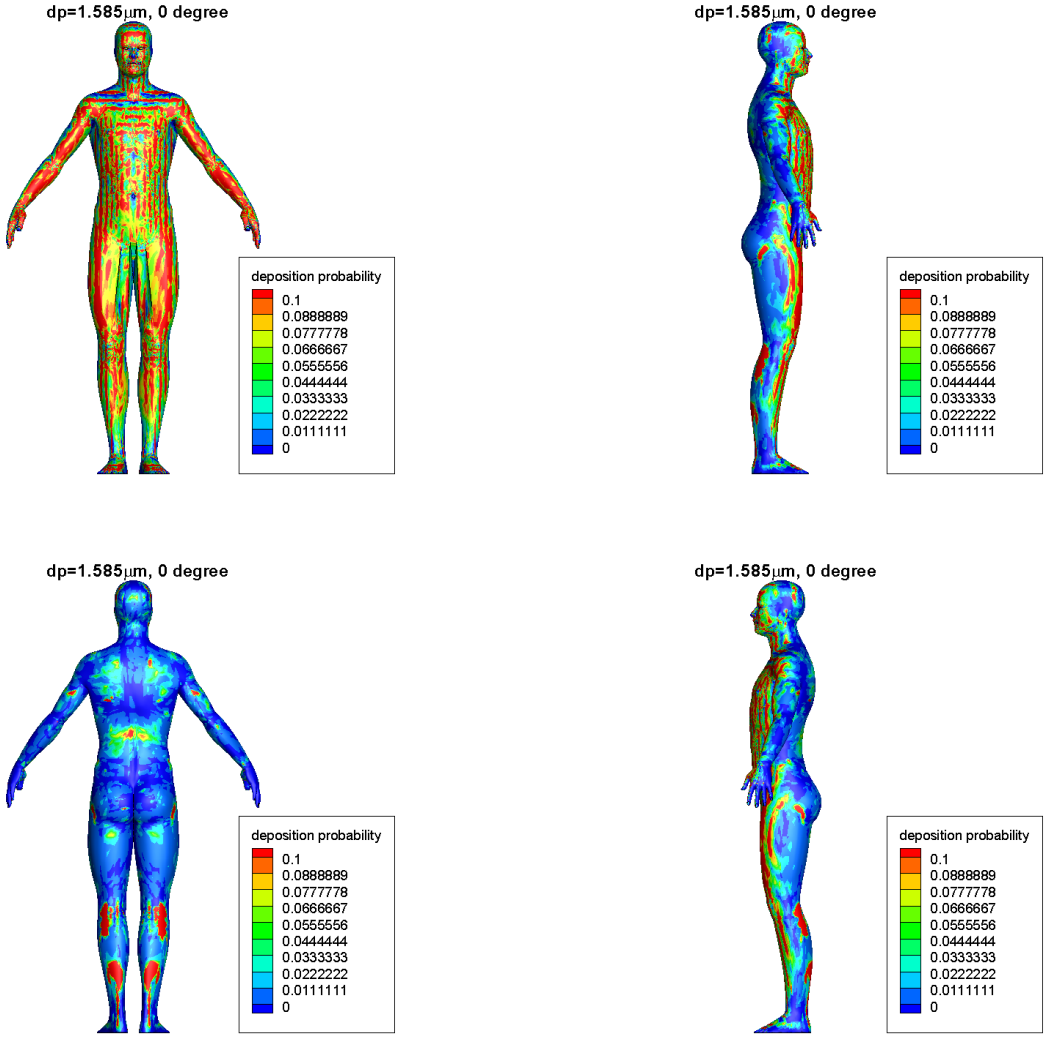

Figure 4.18: Isopleths of the deposition probability for a particle diameter of $d_p = 1.585$ μm for the human form oriented at 0 degree with respect to the incident wind direction.

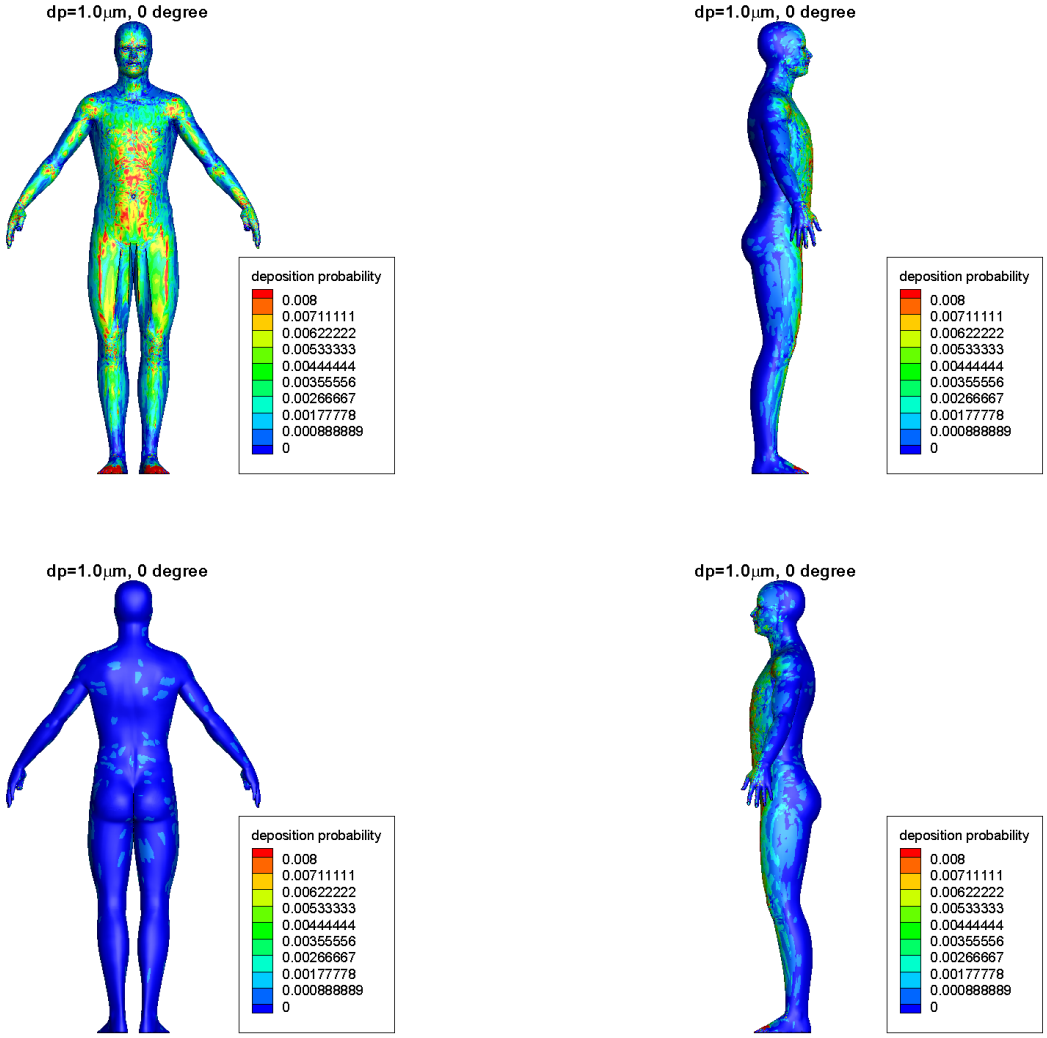

Figure 4.19: Isopleths of the deposition probability for a particle diameter of $d_p = 1.0$ μm for the human form oriented at 0 degree with respect to the incident wind direction.

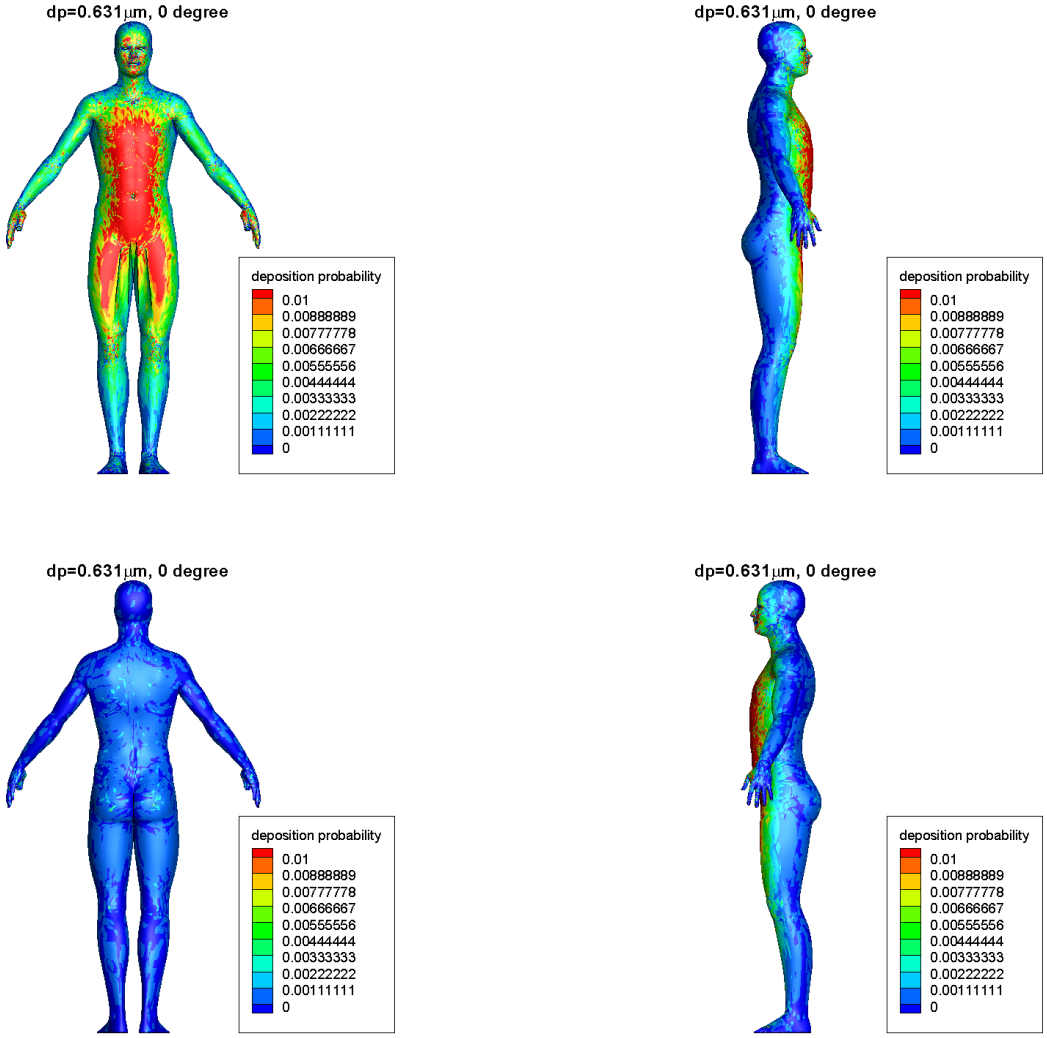

Figure 4.20: Isopleths of the deposition probability for a particle diameter of $d_p = 0.631$ μm for the human form oriented at 0 degree with respect to the incident wind direction.

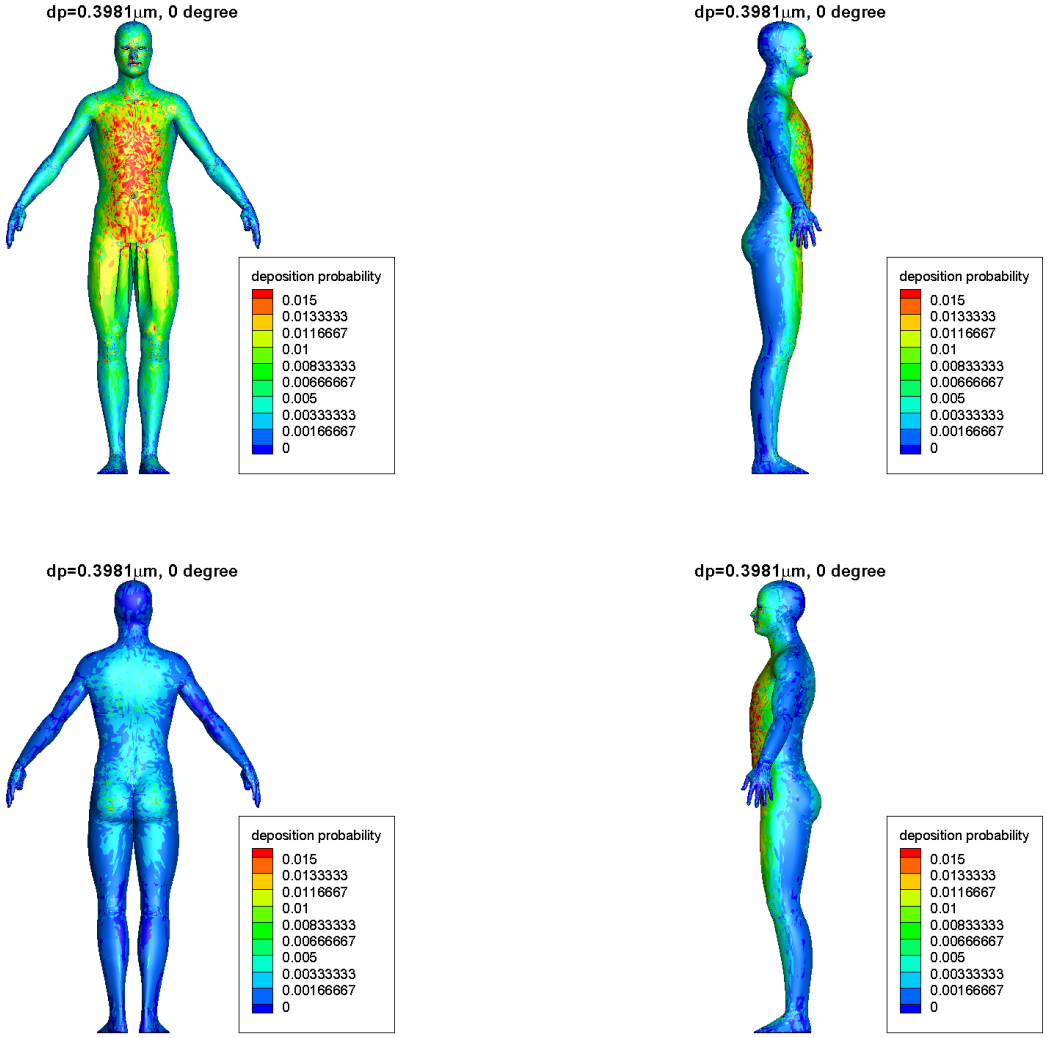

Figure 4.21: Isopleths of the deposition probability for a particle diameter of $d_p = 0.3981$ μm for the human form oriented at 0 degree with respect to the incident wind direction.

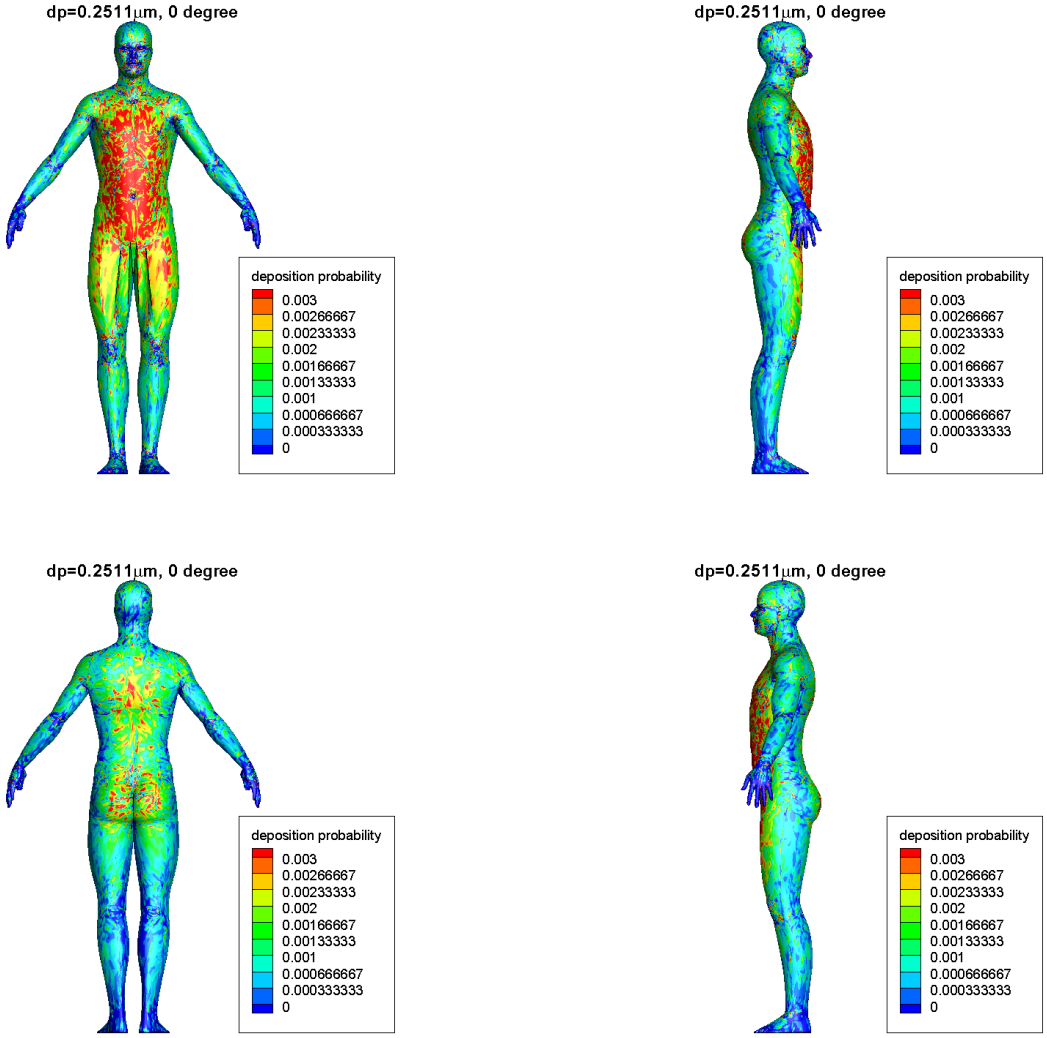

Figure 4.22: Isopleths of the deposition probability for a particle diameter of $d_p = 0.2511$ μm for the human form oriented at 0 degree with respect to the incident wind direction.

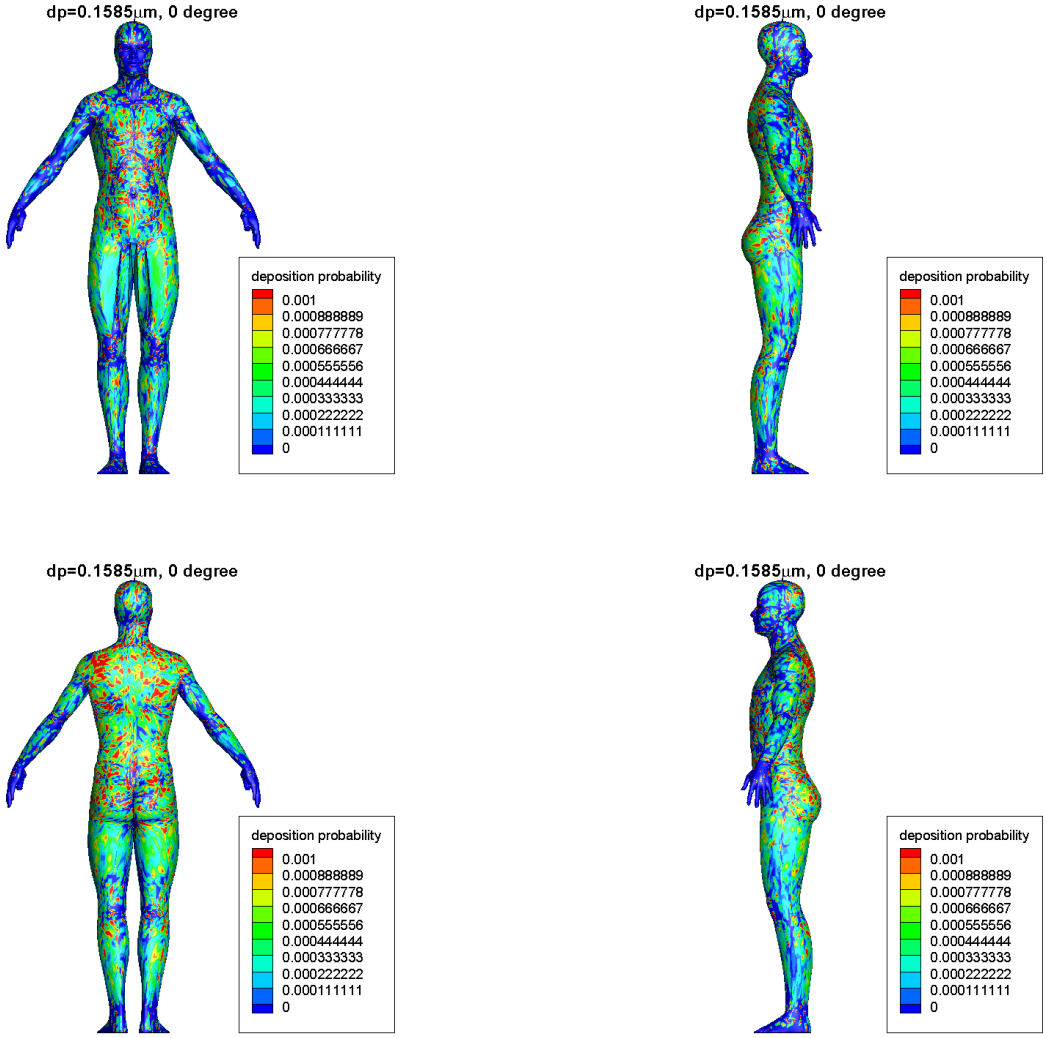

Figure 4.23: Isopleths of the deposition probability for a particle diameter of $d_p = 0.1585$ μm for the human form oriented at 0 degree with respect to the incident wind direction.

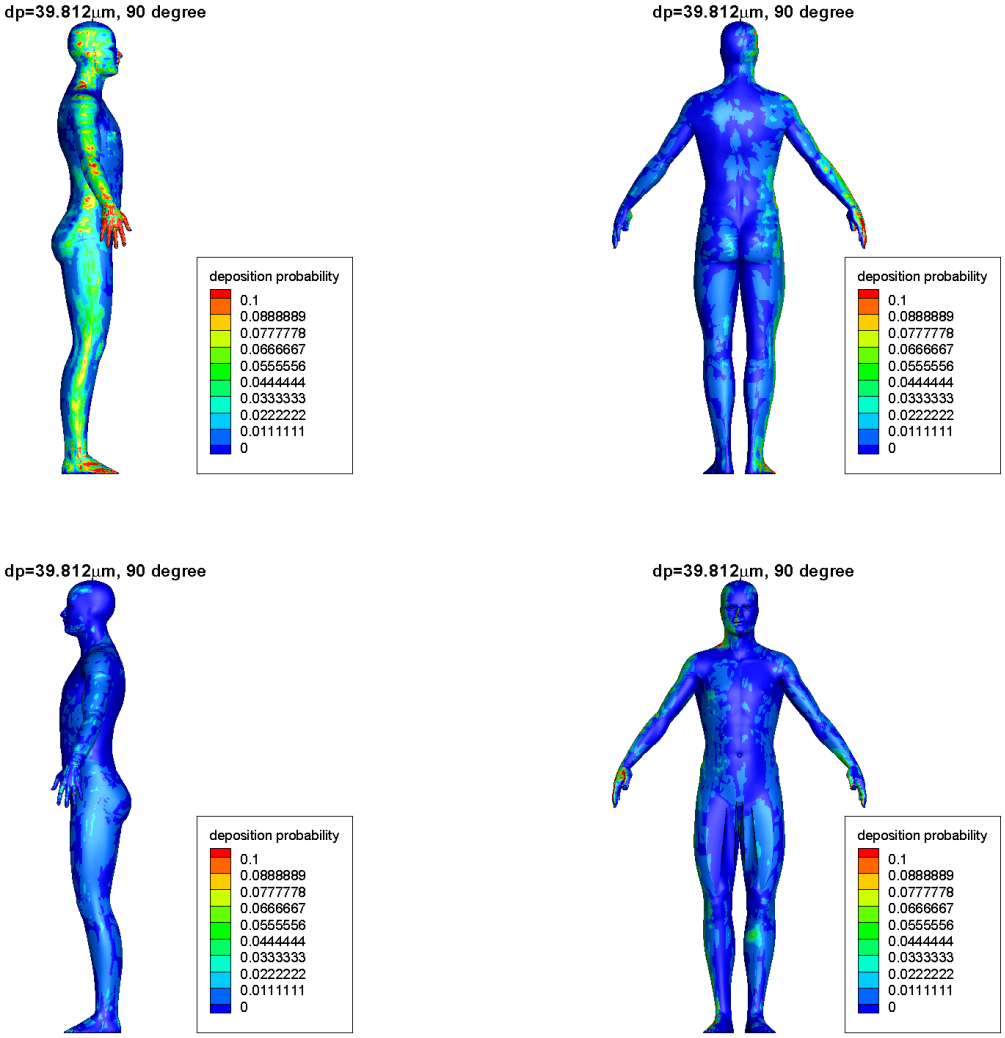

Figure 4.24: Isopleths of the deposition probability for a particle diameter of $d_p = 39.812$ μm for the human form oriented at 90 degree with respect to the incident wind direction.

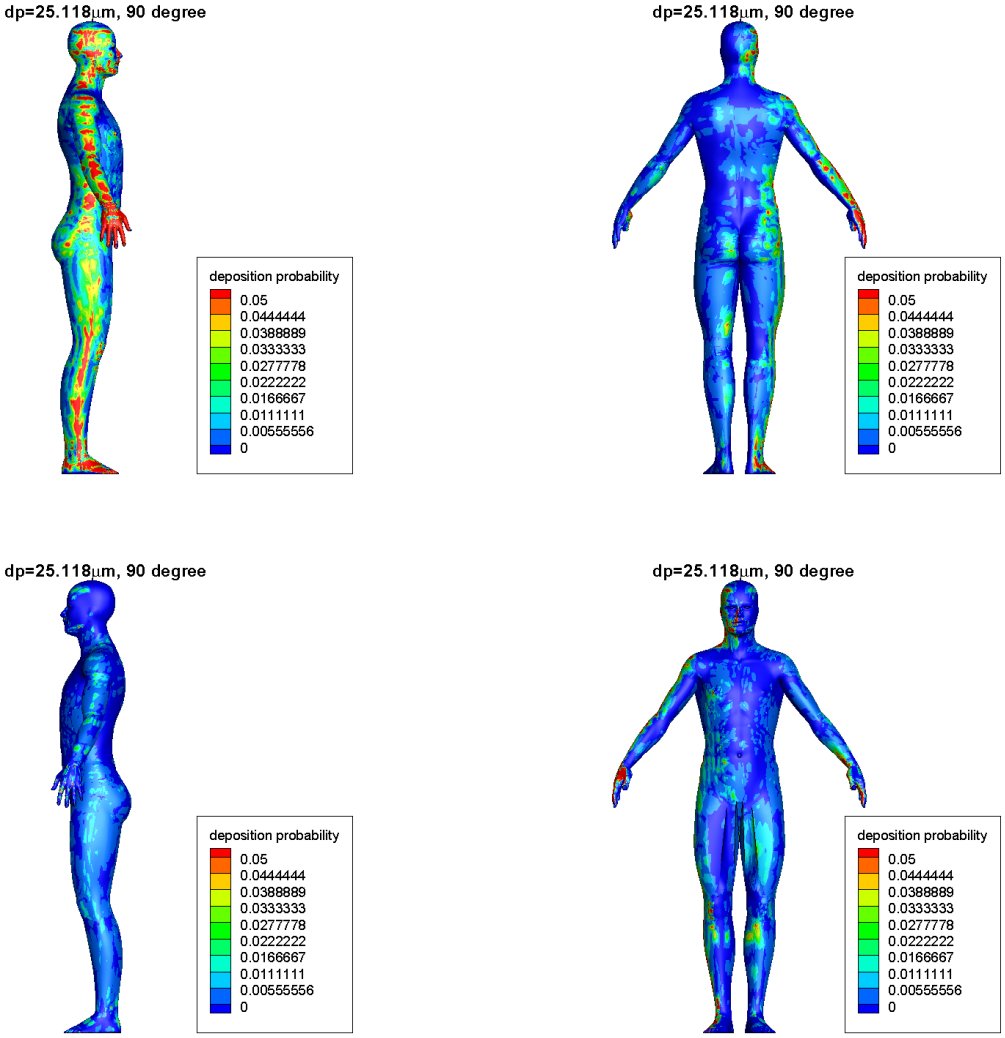

Figure 4.25: Isopleths of the deposition probability for a particle diameter of $d_p = 25.118$ μm for the human form oriented at 90 degree with respect to the incident wind direction.

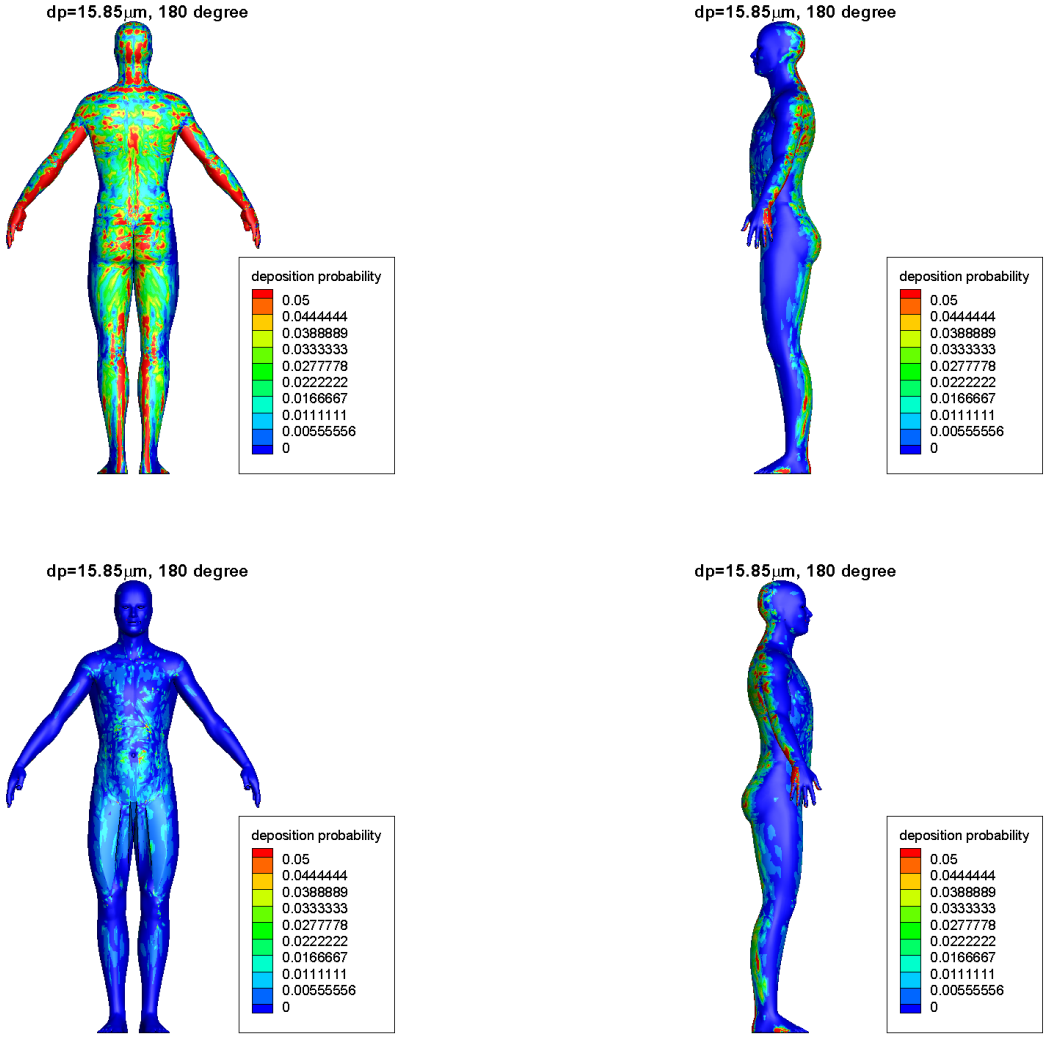

Figure 4.26: Isopleths of the deposition probability for a particle diameter of $d_p = 15.85$ μm for the human form oriented at 90 degree with respect to the incident wind direction.

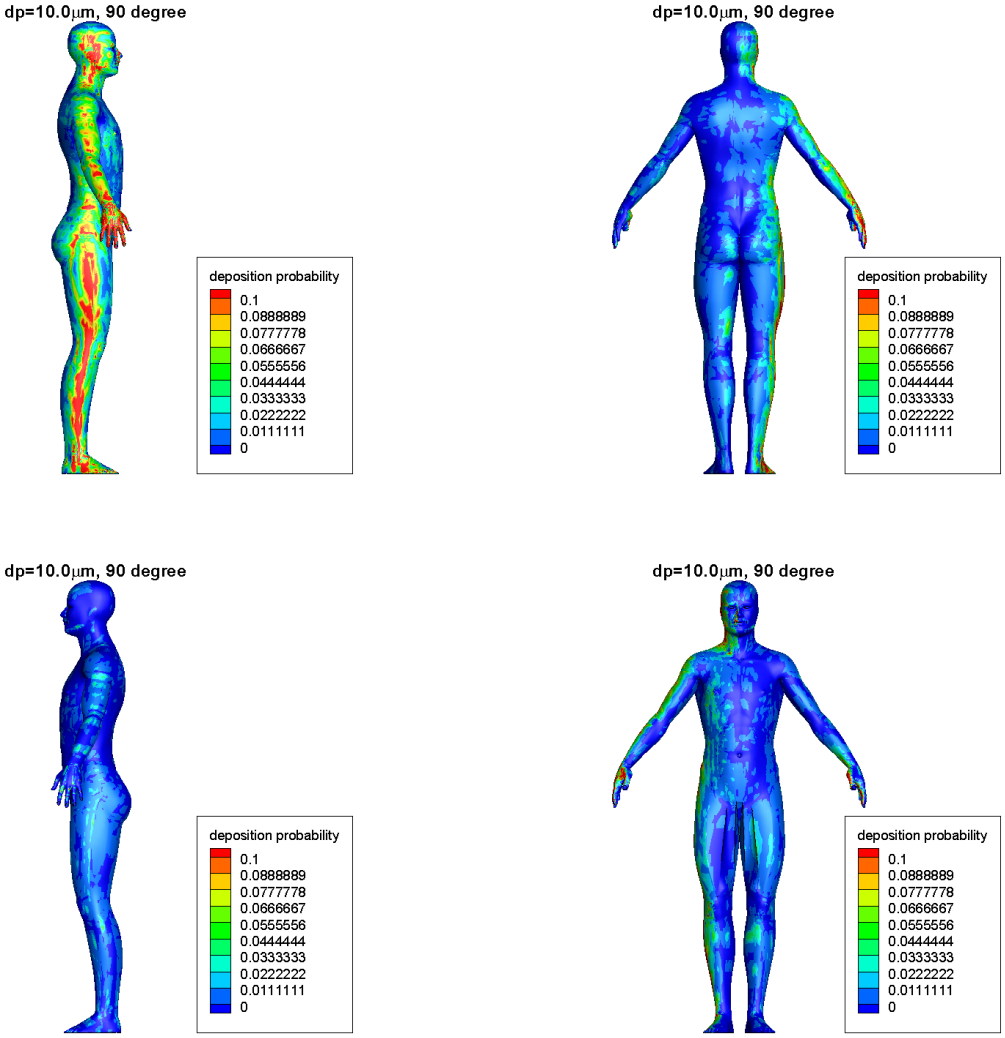

Figure 4.27: Isopleths of the deposition probability for a particle diameter of $d_p = 10.0$ μm for the human form oriented at 90 degree with respect to the incident wind direction.

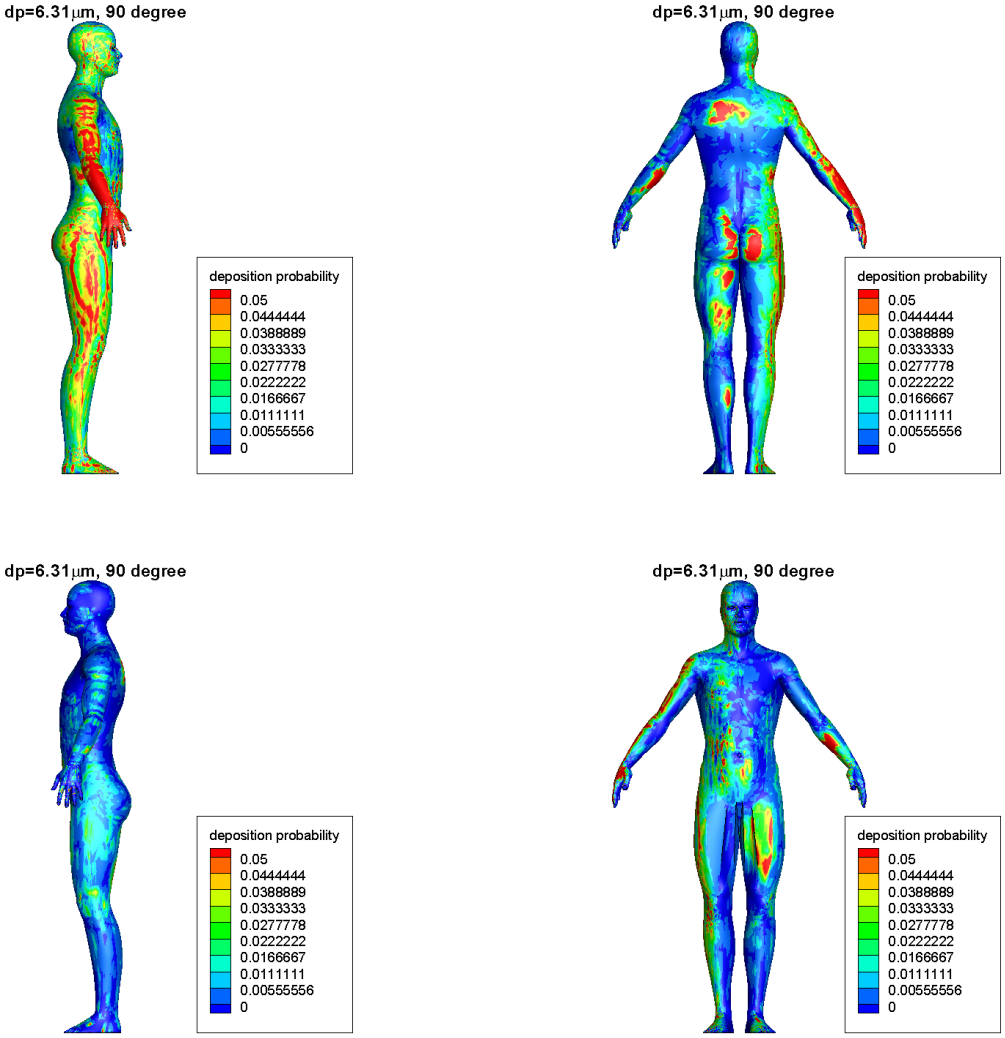

Figure 4.28: Isopleths of the deposition probability for a particle diameter of $d_p = 6.31$ μm for the human form oriented at 90 degree with respect to the incident wind direction.

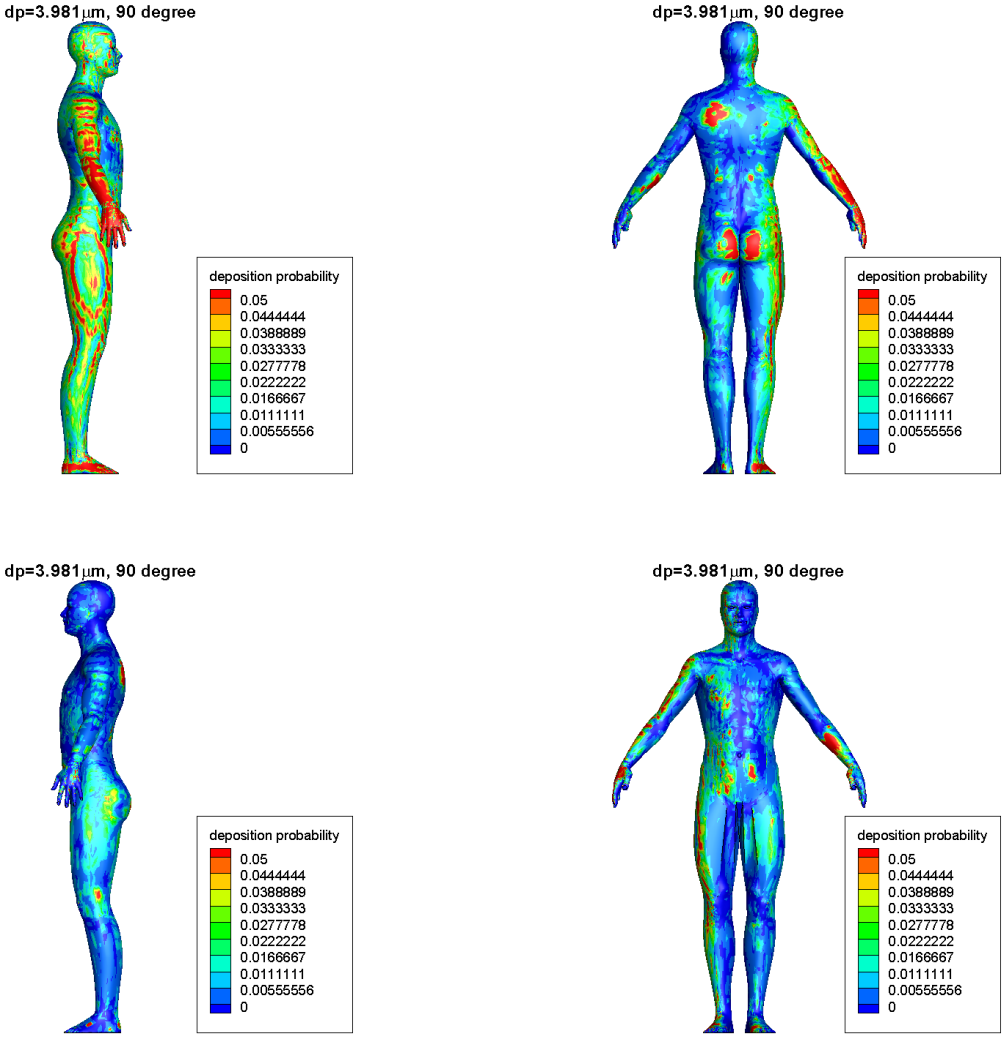

Figure 4.29: Isopleths of the deposition probability for a particle diameter of $d_p = 3.981$ μm for the human form oriented at 90 degree with respect to the incident wind direction.

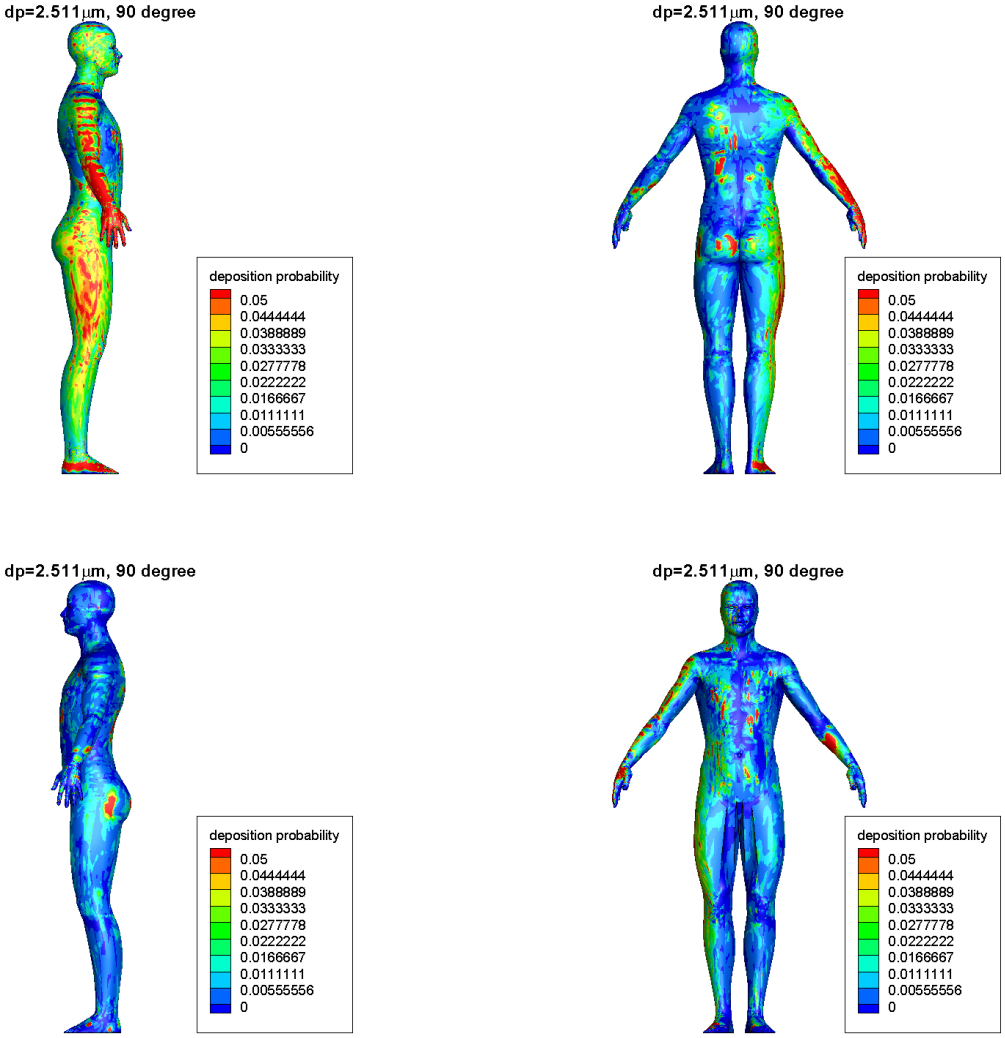

Figure 4.30: Isopleths of the deposition probability for a particle diameter of $d_p = 2.511$ μm for the human form oriented at 90 degree with respect to the incident wind direction.

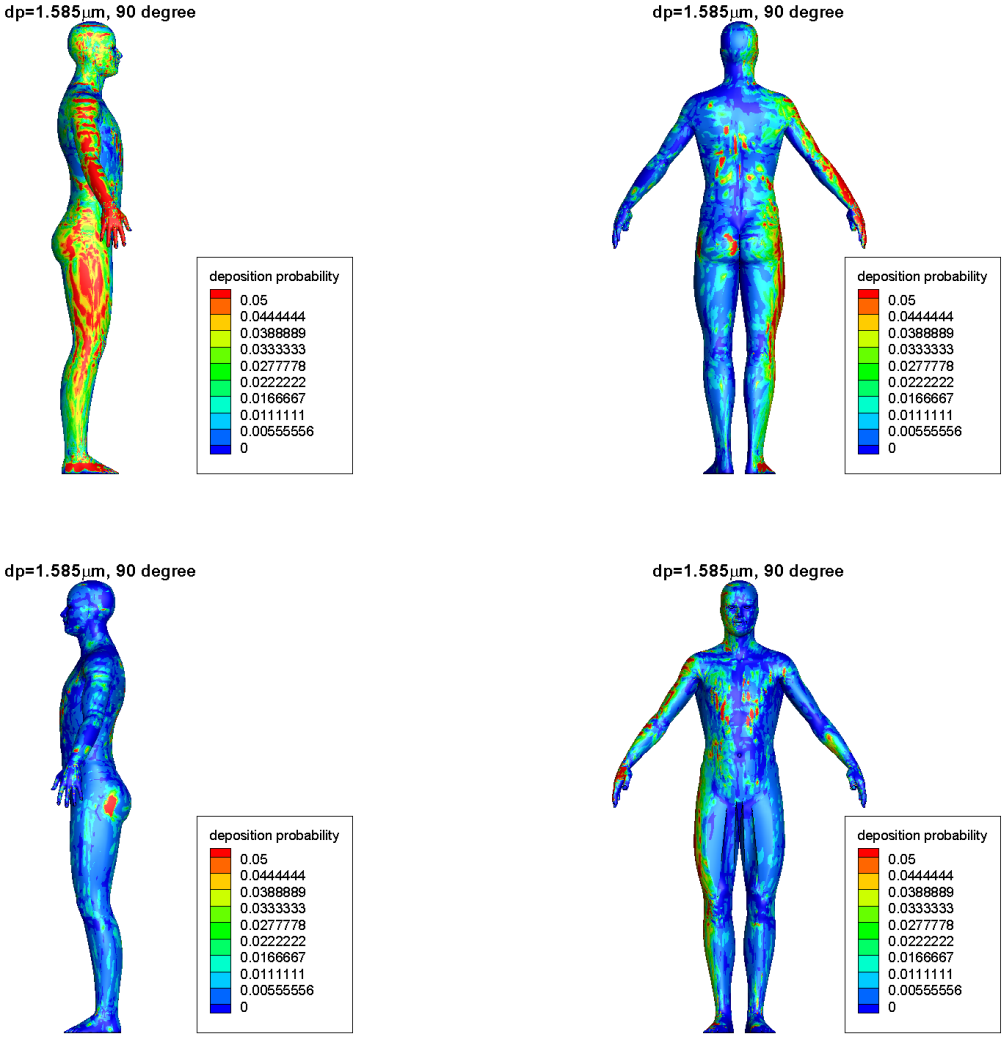

Figure 4.31: Isopleths of the deposition probability for a particle diameter of $d_p = 1.585$ μm for the human form oriented at 90 degree with respect to the incident wind direction.

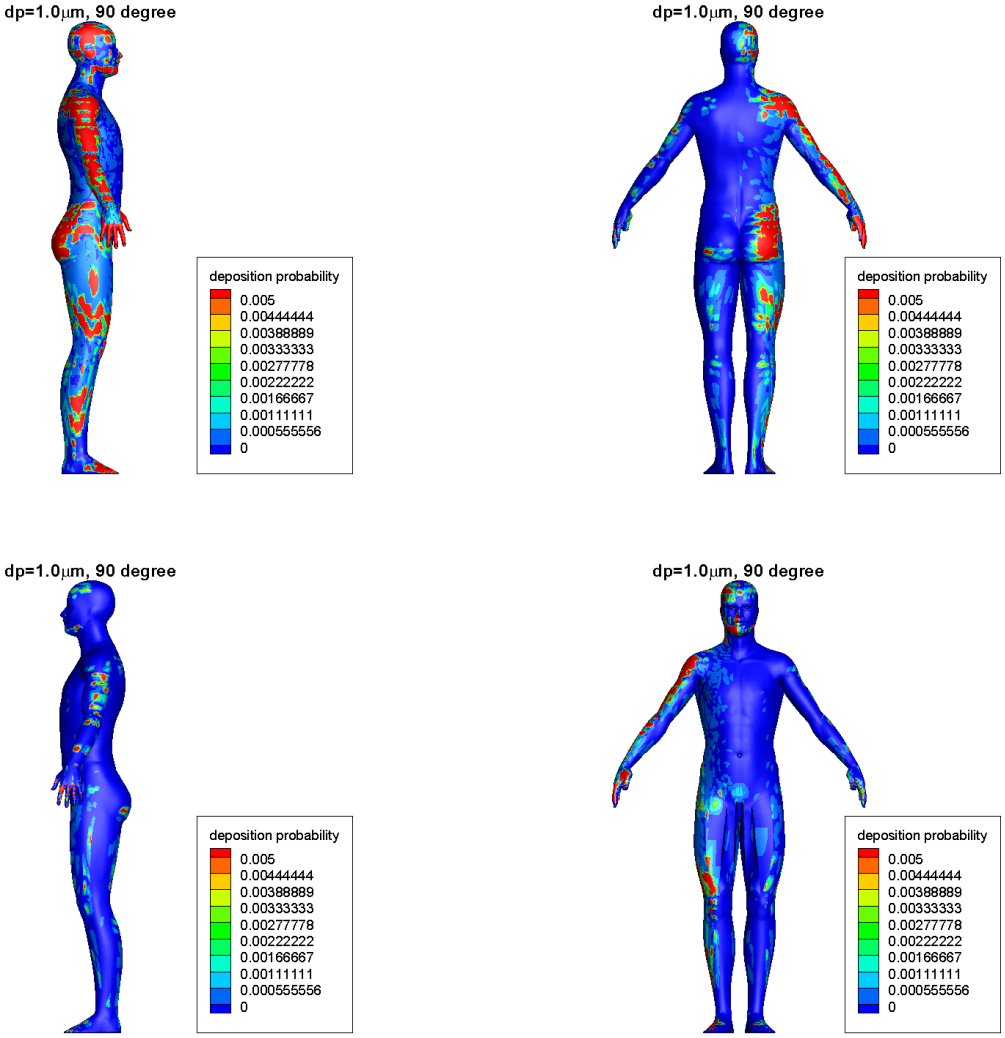

Figure 4.32: Isopleths of the deposition probability for a particle diameter of $d_p = 1.0$ μm for the human form oriented at 90 degree with respect to the incident wind direction..

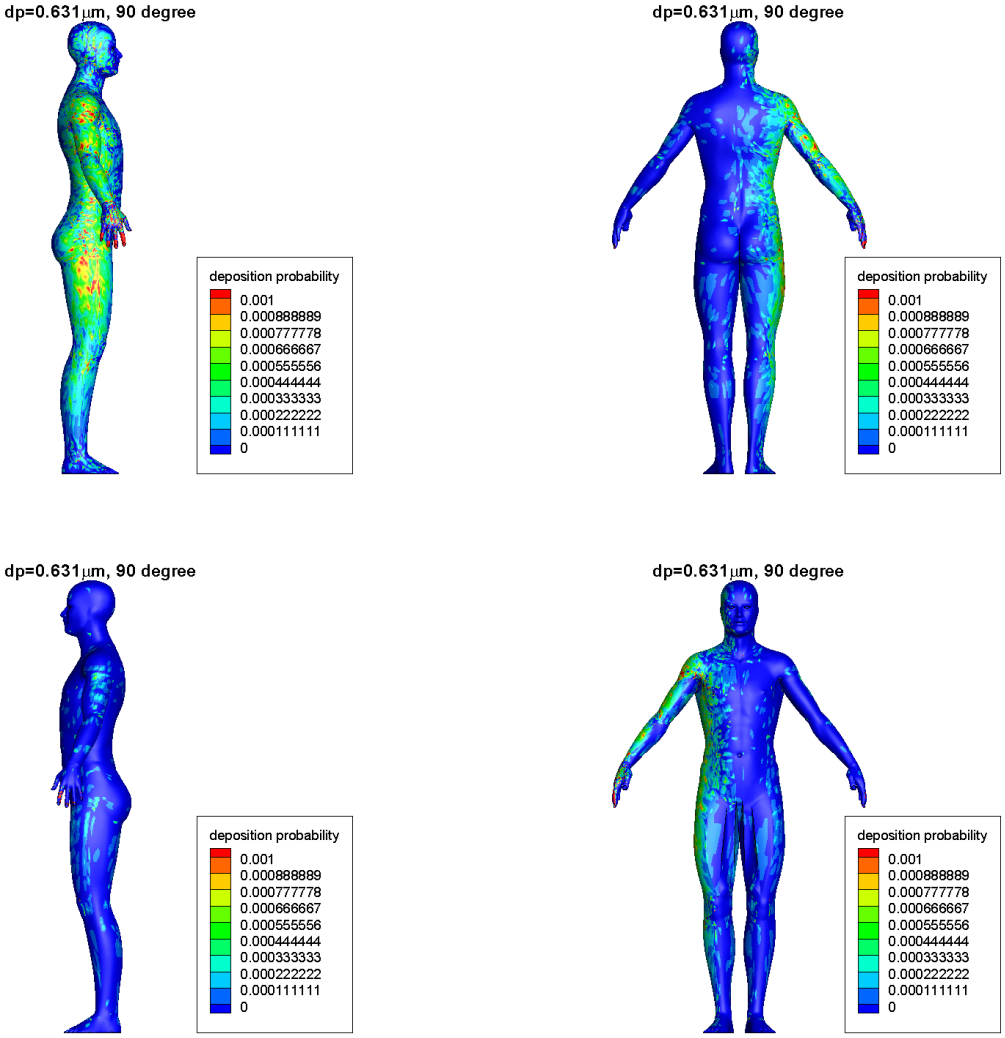

Figure 4.33: Isopleths of the deposition probability for a particle diameter of $d_p = 0.631$ μm for the human form oriented at 90 degree with respect to the incident wind direction.

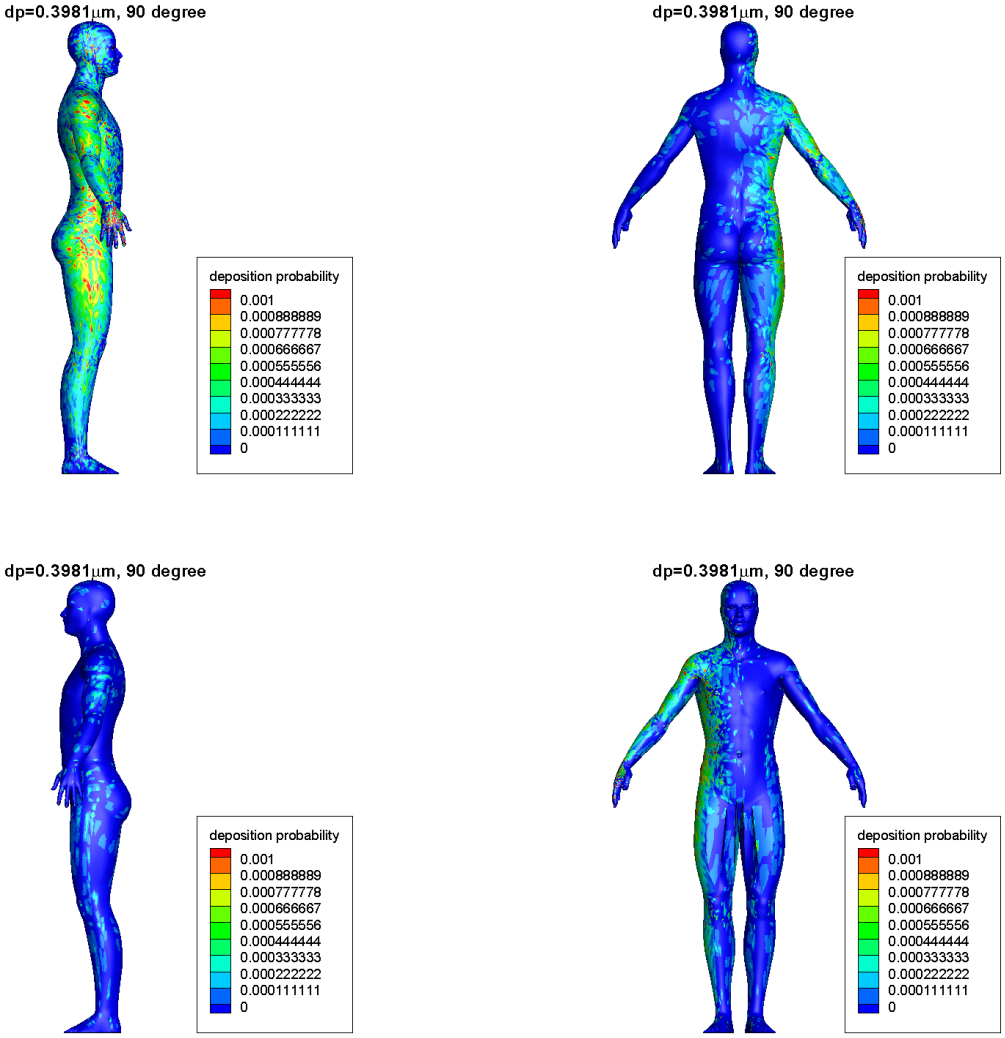

Figure 4.34: Isopleths of the deposition probability for a particle diameter of $d_p = 0.3981$ μm for the human form oriented at 90 degree with respect to the incident wind direction.

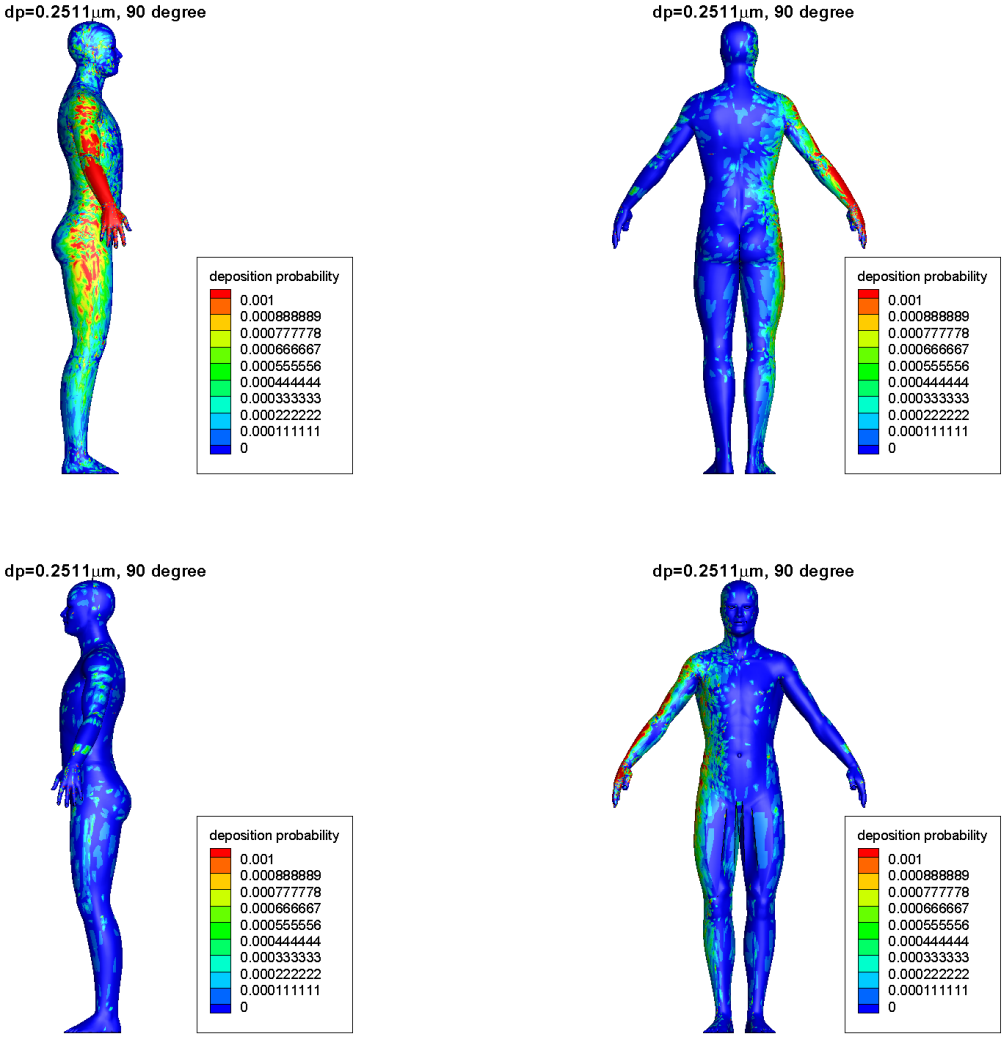

Figure 4.35: Isopleths of the deposition probability for a particle diameter of $d_p = 0.2511$ μm for the human form oriented at 90 degree with respect to the incident wind direction.

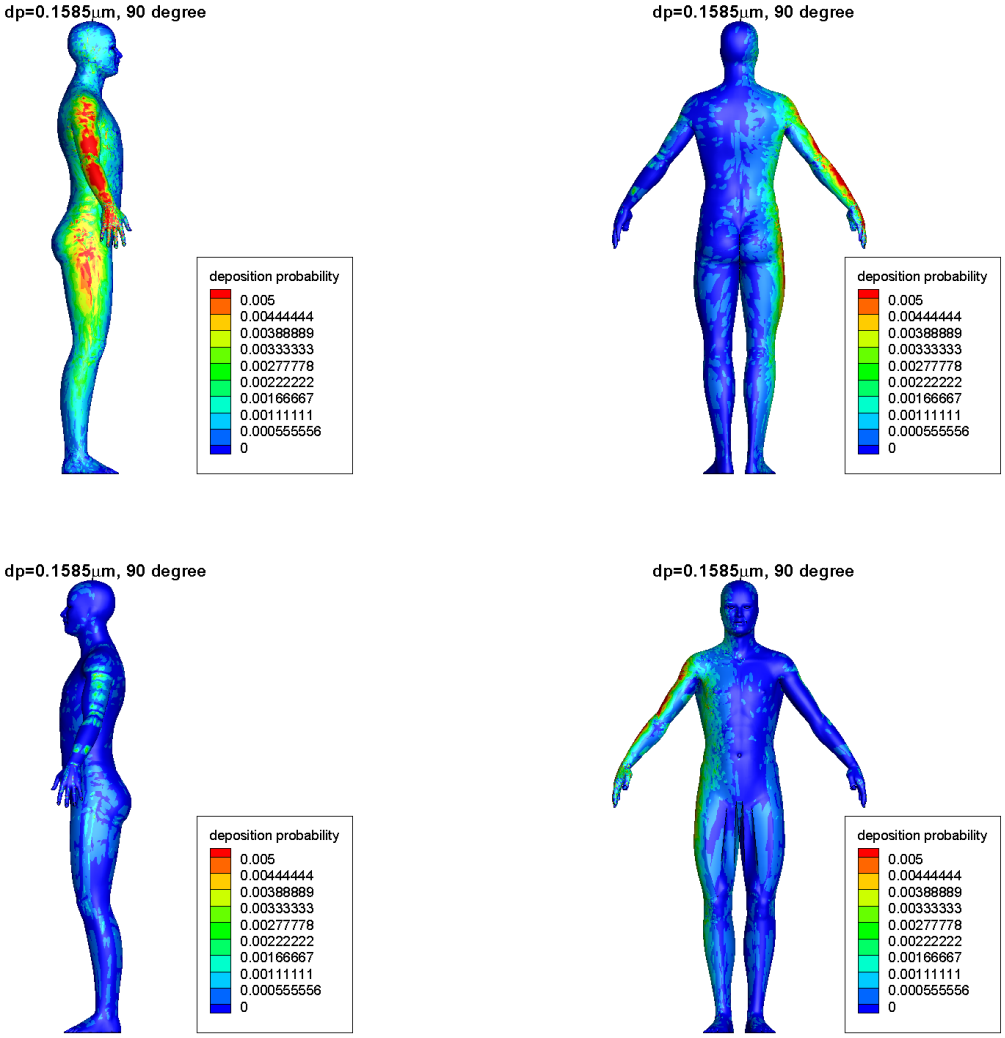

Figure 4.36: Isopleths of the deposition probability for a particle diameter of $d_p = 0.1585$ μm for the human form oriented at 90 degree with respect to the incident wind direction.

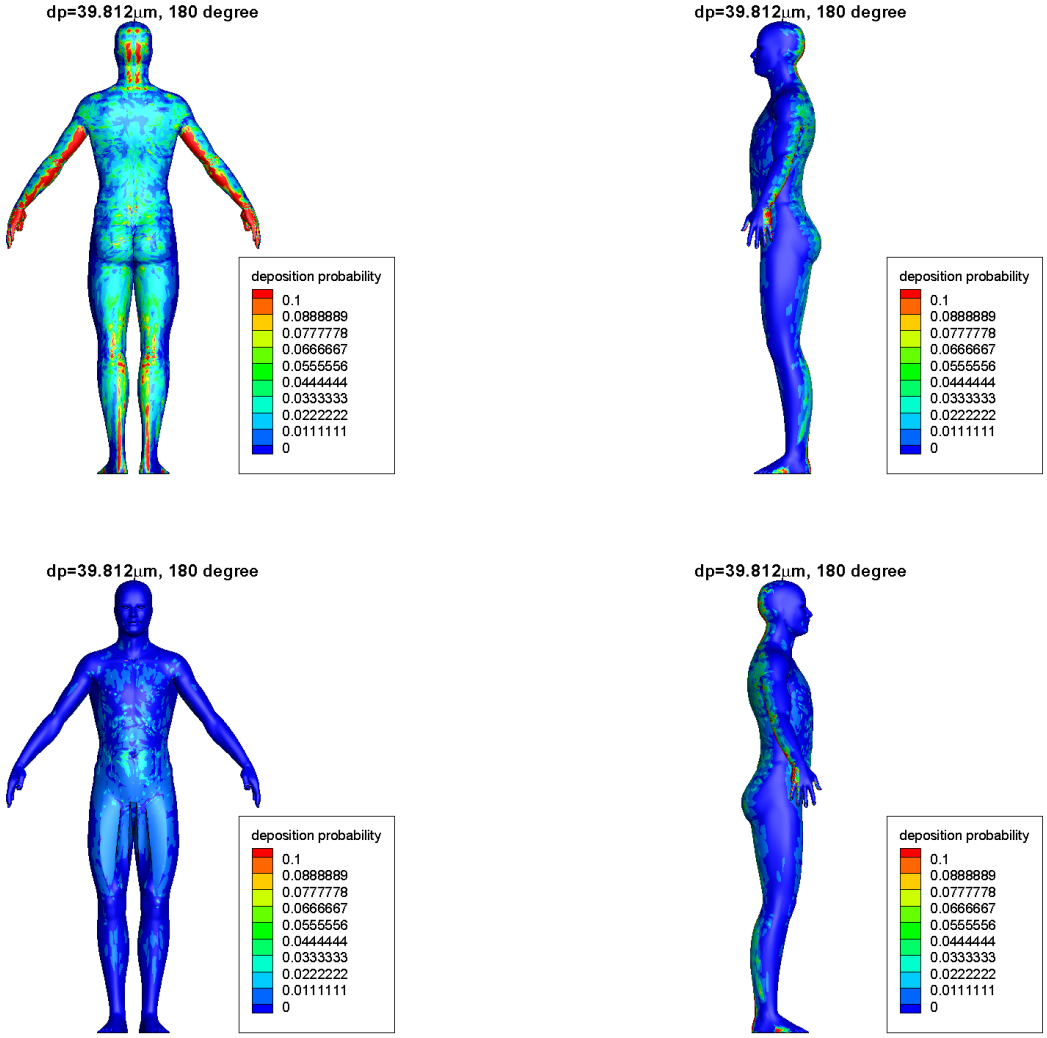

Figure 4.37: Isopleths of the deposition probability for a particle diameter of $d_p = 39.812$ μm for the human form oriented at 180 degree with respect to the incident wind direction.

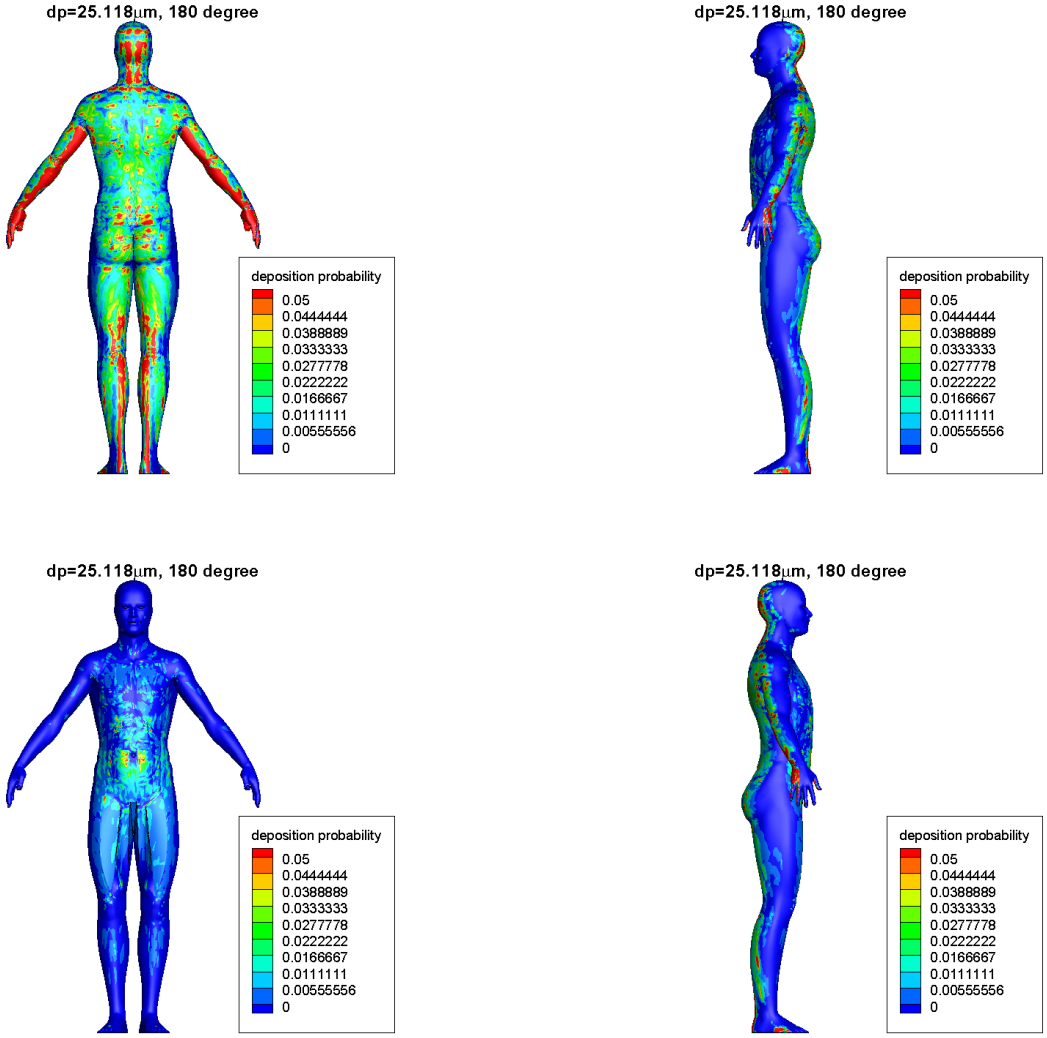

Figure 4.38: Isopleths of the deposition probability for a particle diameter of $d_p = 25.118$ μm for the human form oriented at 180 degree with respect to the incident wind direction.

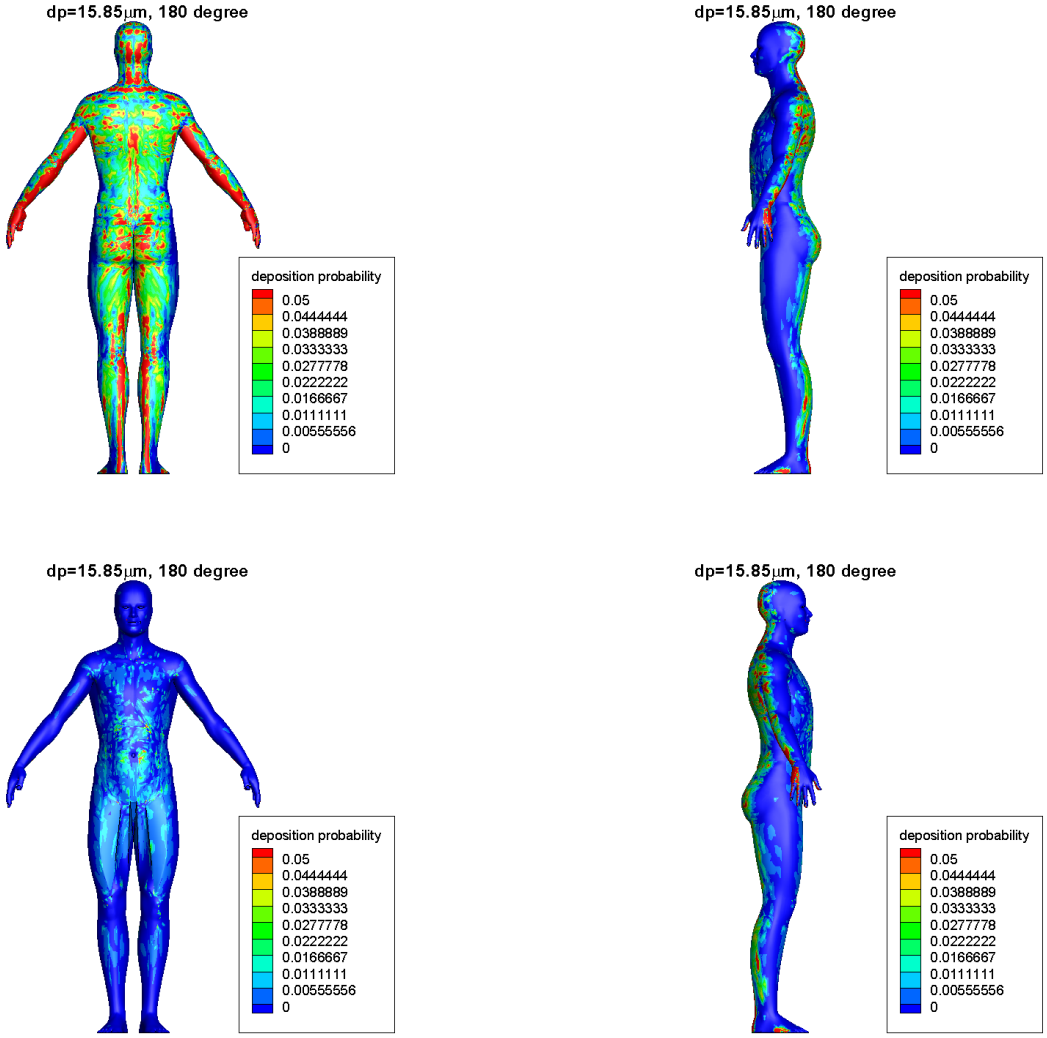

Figure 4.39: Isopleths of the deposition probability for a particle diameter of $d_p = 15.85$ μm for the human form oriented at 180 degree with respect to the incident wind direction.

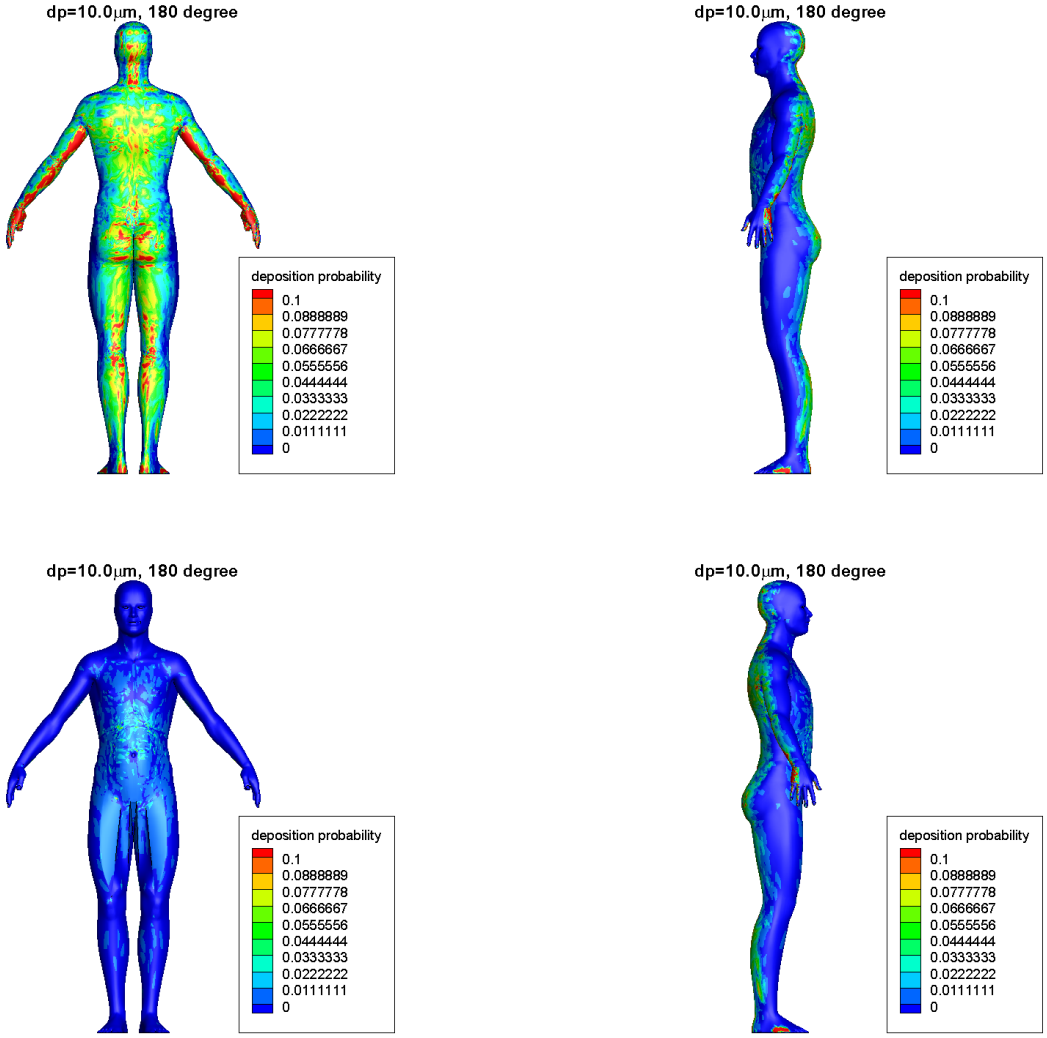

Figure 4.40: Isopleths of the deposition probability for a particle diameter of $d_p = 10.0$ μm for the human form oriented at 180 degree with respect to the incident wind direction.

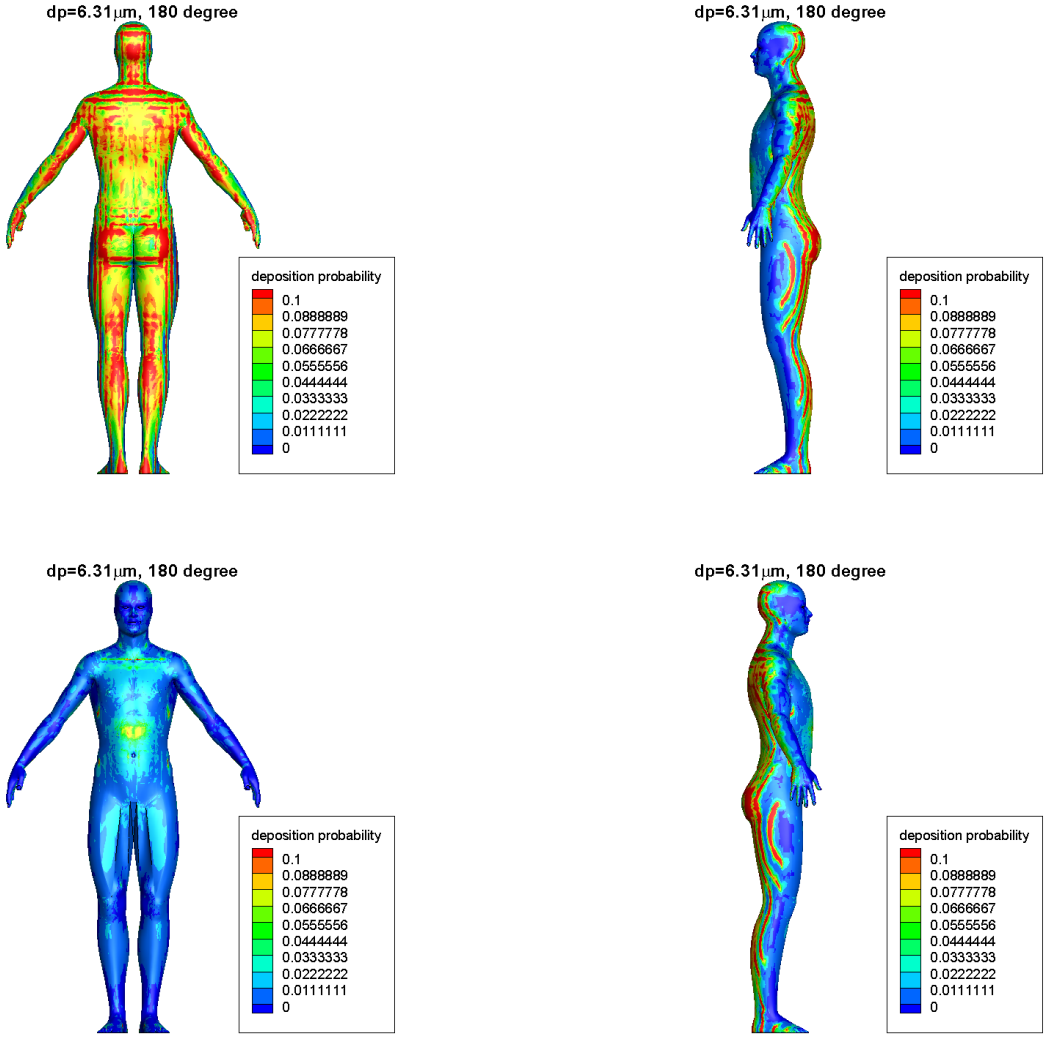

Figure 4.41: Isopleths of the deposition probability for a particle diameter of $d_p = 6.31$ μm for the human form oriented at 180 degree with respect to the incident wind direction.

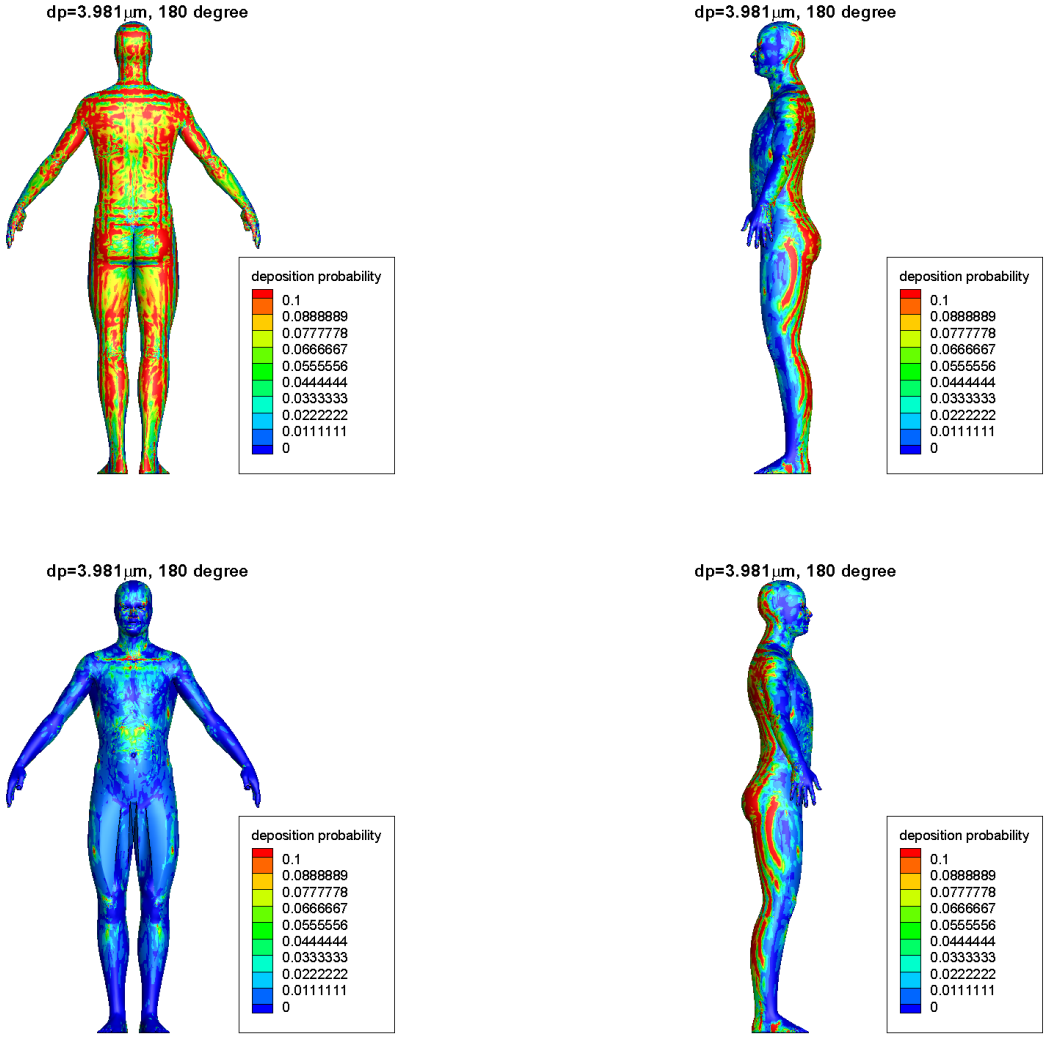

Figure 4.42: Isopleths of the deposition probability for a particle diameter of $d_p = 3.981$ μm for the human form oriented at 180 degree with respect to the incident wind direction.

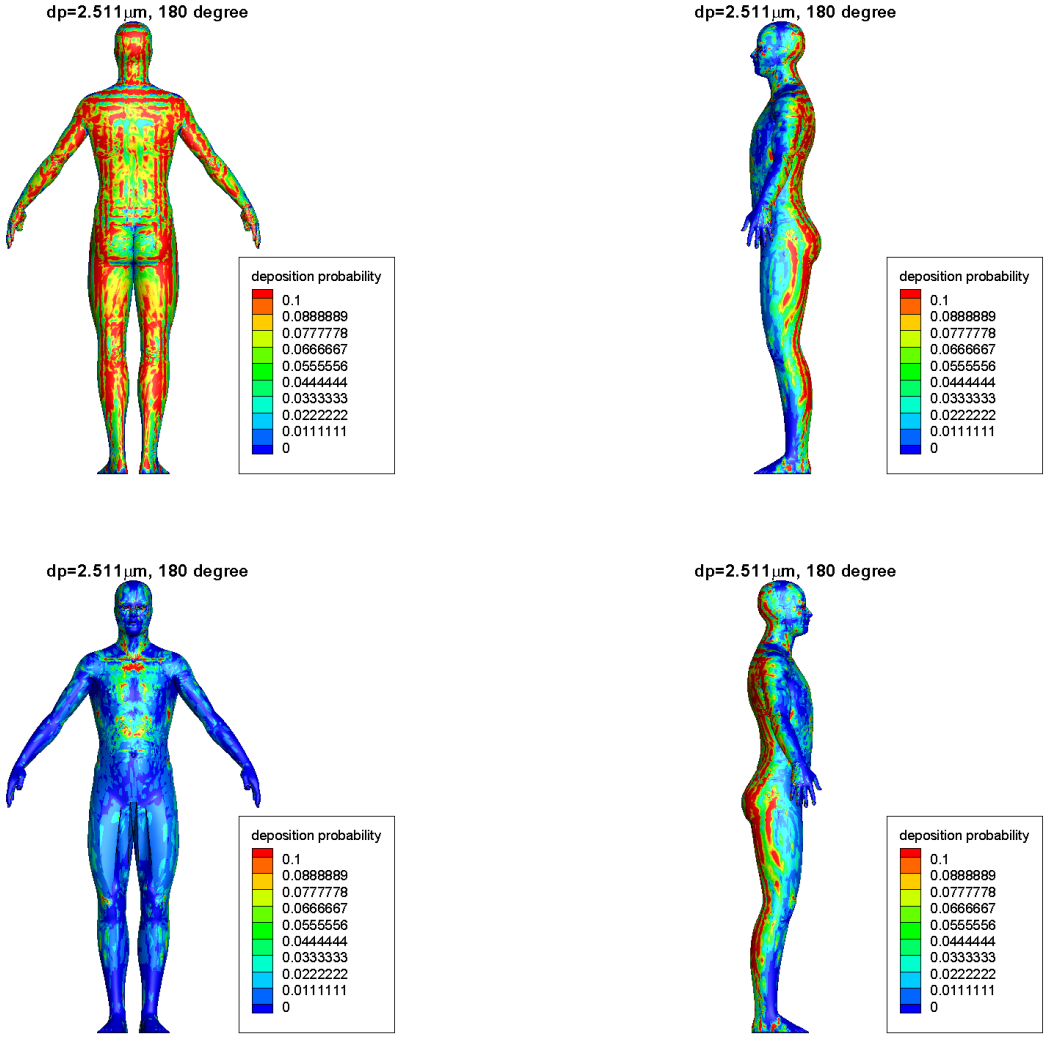

Figure 4.43: Isopleths of the deposition probability for a particle diameter of $d_p = 2.511$ μm for the human form oriented at 180 degree with respect to the incident wind direction..

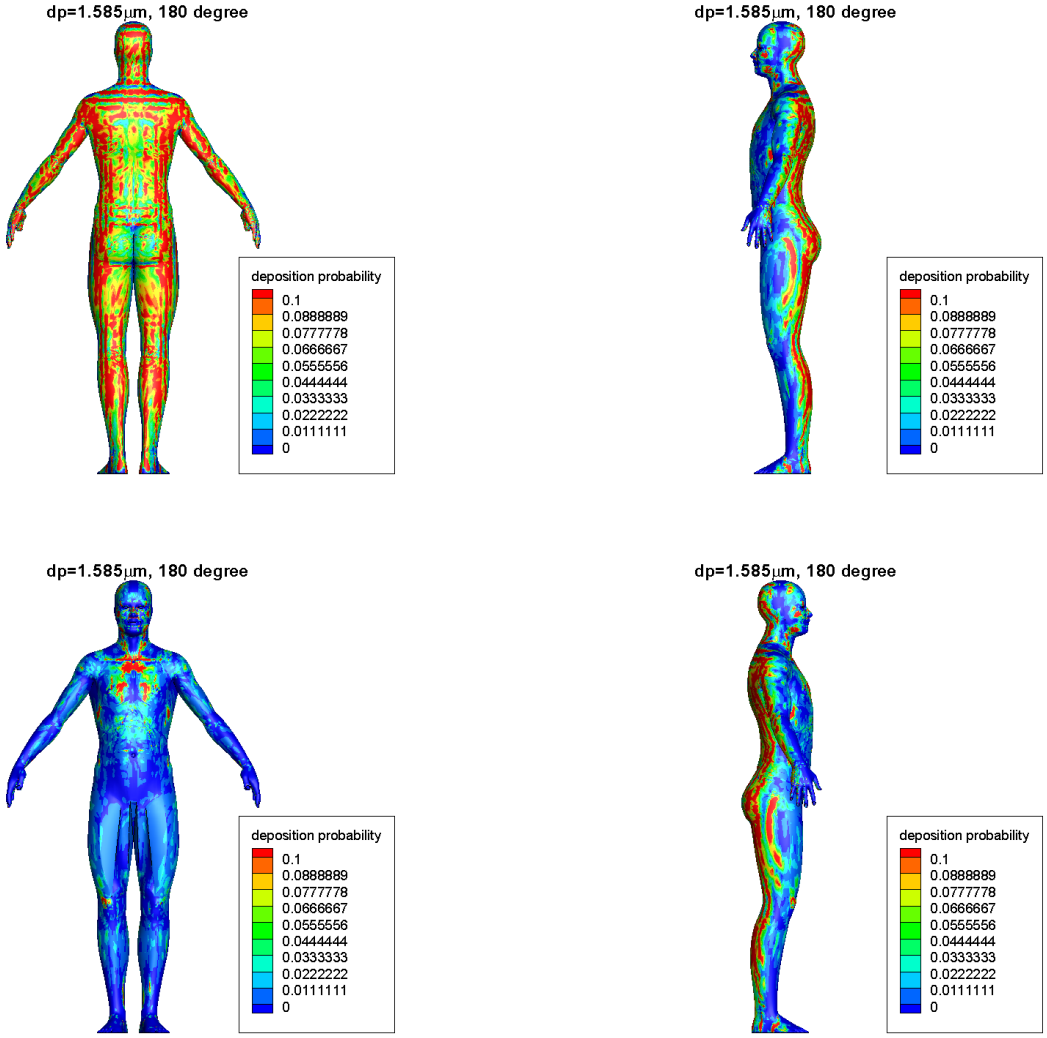

Figure 4.44: Isopleths of the deposition probability for a particle diameter of $d_p = 1.585$ μm for the human form oriented at 180 degree with respect to the incident wind direction.

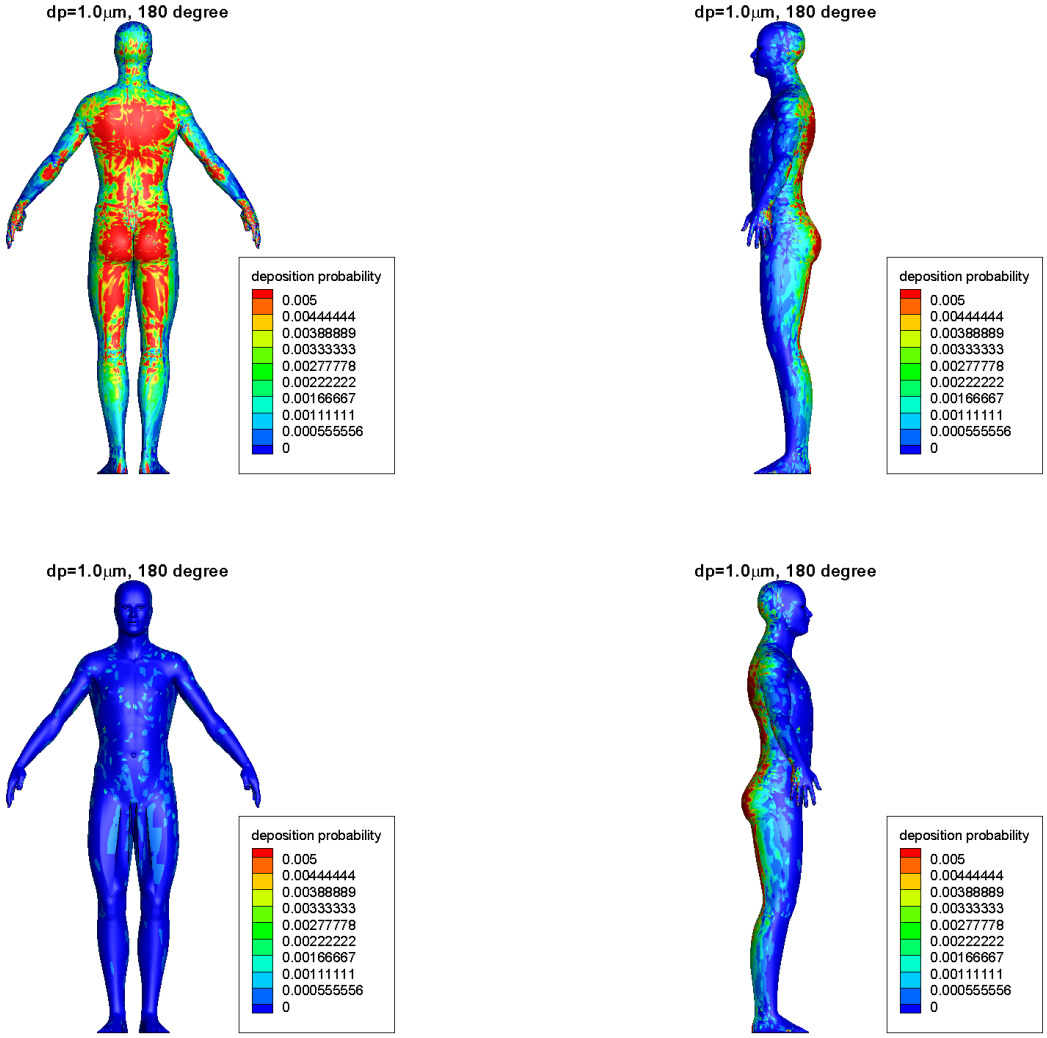

Figure 4.45: Isopleths of the deposition probability for a particle diameter of $d_p = 1.0$ μm for the human form oriented at 180 degree with respect to the incident wind direction.

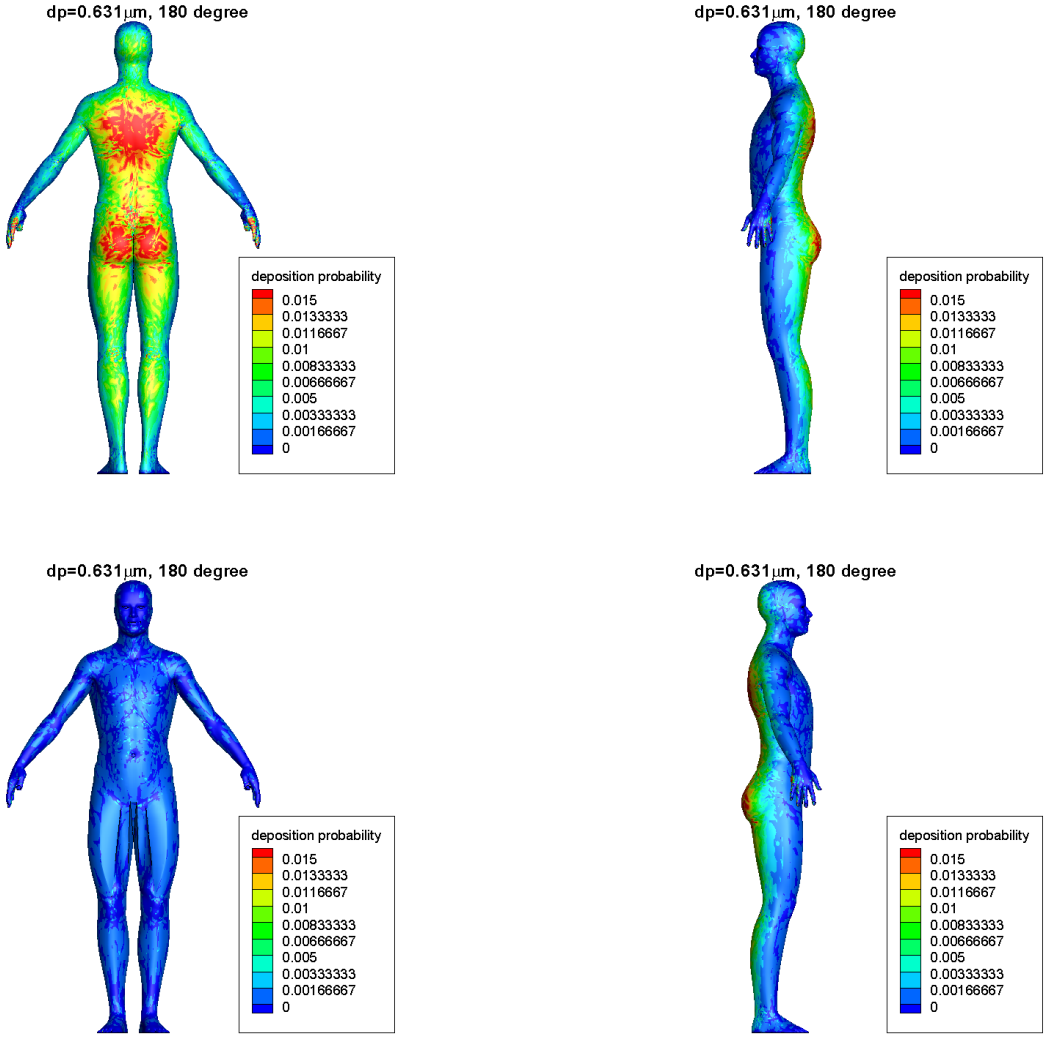

Figure 4.46: Isopleths of the deposition probability for a particle diameter of $d_p = 0.631$ μm for the human form oriented at 180 degree with respect to the incident wind direction.

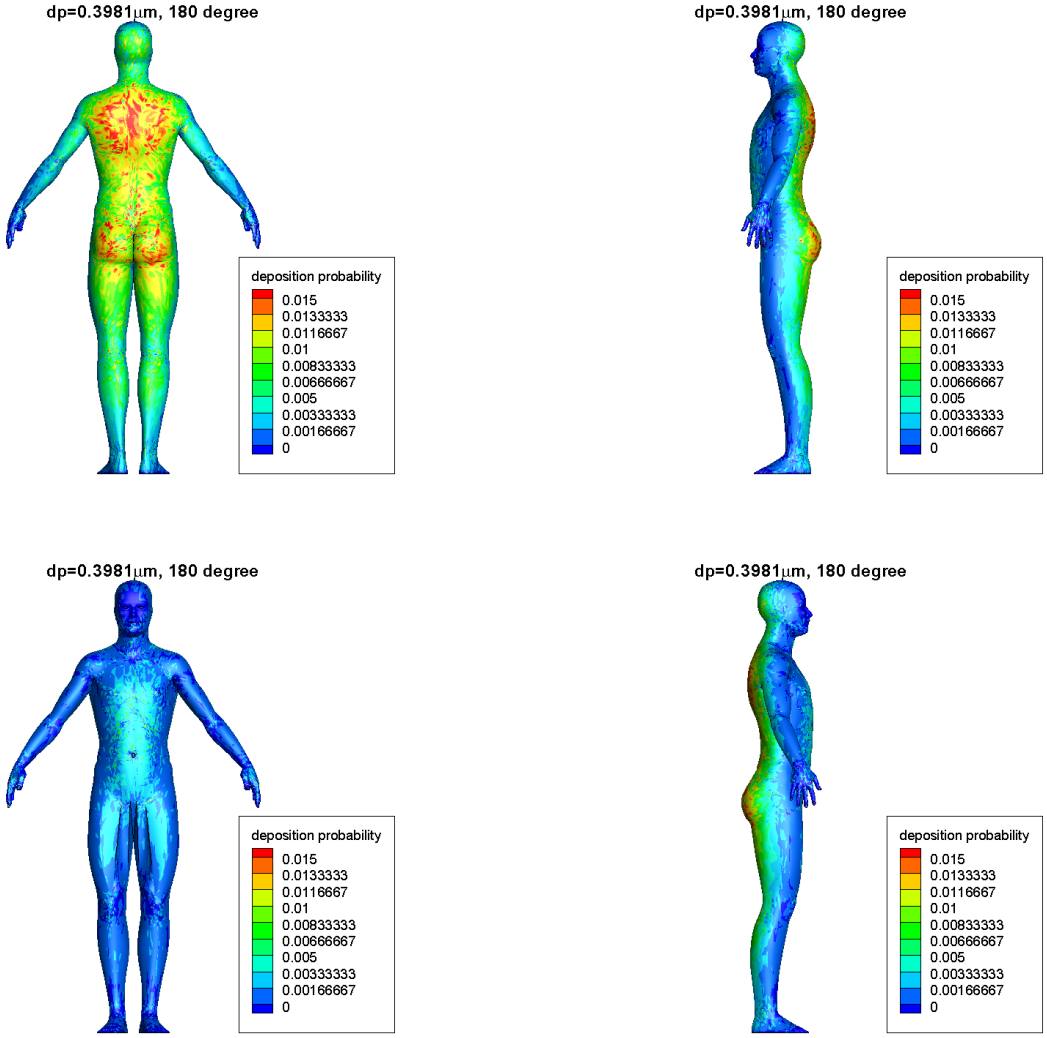

Figure 4.47: Isopleths of the deposition probability for a particle diameter of $d_p = 0.3981$ μm for the human form oriented at 180 degree with respect to the incident wind direction.

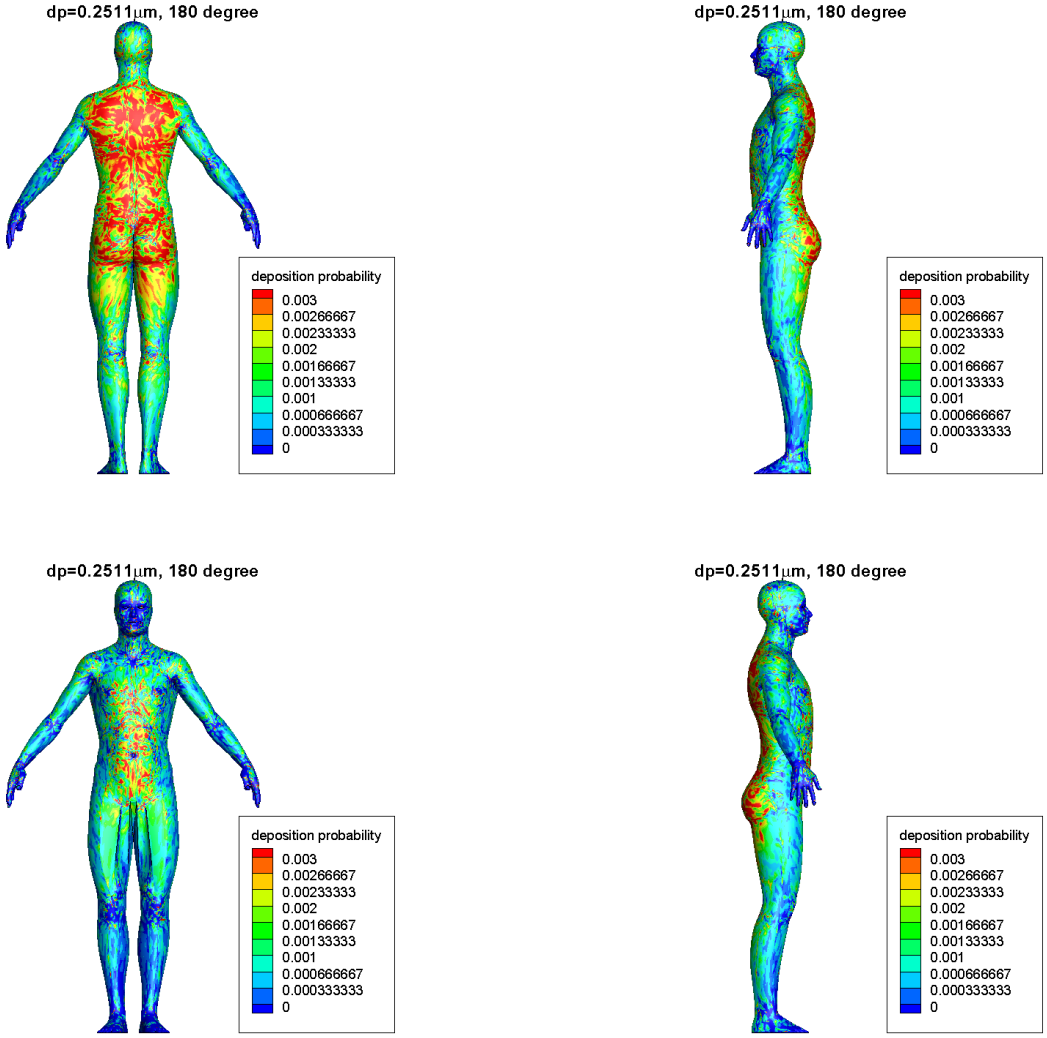

Figure 4.48: Isopleths of the deposition probability for a particle diameter of $d_p = 0.2511$ μm for the human form oriented at 180 degree with respect to the incident wind direction.

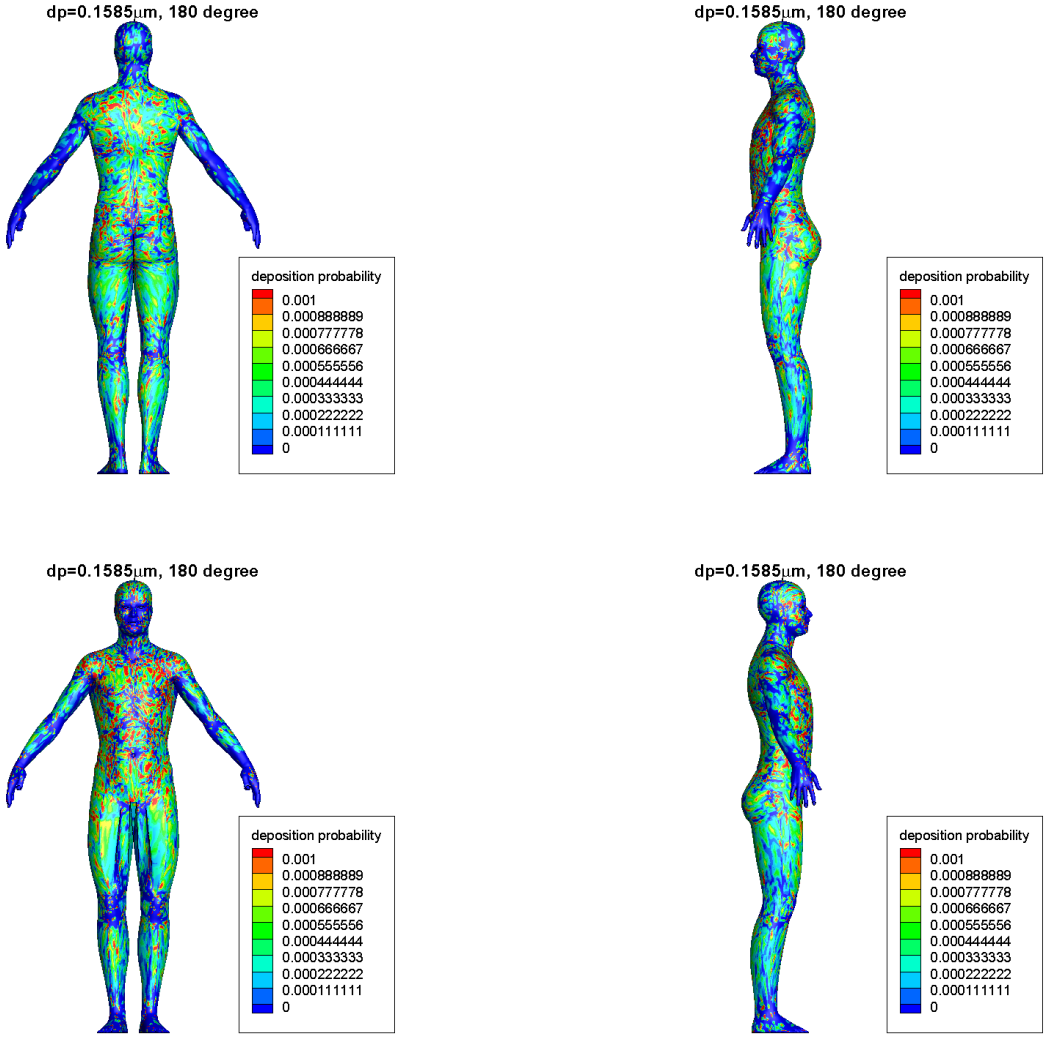

Figure 4.49: Isopleths of the deposition probability for a particle diameter of $d_p = 0.1585$ μm for the human form oriented at 180 degree with respect to the incident wind direction.

To provide the quantitative information for the future use by various researchers, we have divided the human body into eleven parts as follows:

1. head (entire),
2. neck (entire),
3. upper chest (including shoulders and down to just below the nipples),
4. lower abdomen (including stomach and down to the waist),
5. arms (both left and right),
6. hands (left and right),
7. legs (left and right, front and back),
8. feet (left and right),
9. back,
10. buttocks,
11. crotch area (frontal area below the waist).

The decomposition of the human form into the various body parts along with their assigned body part indices is shown in Figure 4.50. The following information are provided in the data files that are produced for each of the 39 simulations cases (13 different particle diameters each associated with 3 different orientations of the human form with respect to the incident wind direction):

1. triangular cell number (index),
2. area of the triangular cell (m^2),
3. body index associated with the triangular cell,
4. deposition probability for the triangular cell.

A CD including the data files for each simulation case and a C source code to read the data sets from the files is attached. The Appendix also includes a listing of the C source code. In the CD, there are thirteen directories named in accordance to the particle diameter (i.e., 0p1585, 0p2511, ..., 39p812). In each directory, there are three data files referenced by the orientation angle of the human form relative to the incoming wind direction together

with the particle size. For example, D_000_0P1585.dat is the name of a data file containing information on the deposition probability on the human form for the case associated with a particle diameter of $d_p = 0.1585$ μm with the human form oriented at 0 degree with respect to the incident wind direction; similarly, D_090_6P31.dat is the name of a data file containing deposition probability on the human form for the case associated with a particle diameter of $d_p = 6.31$ μm with the human form oriented at 90 degrees with respect to the incident wind direction.

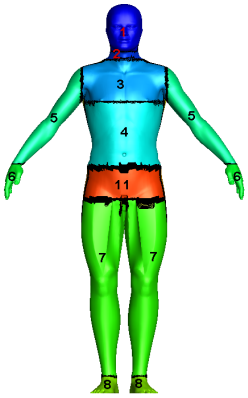

(a)

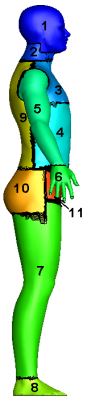

(b)

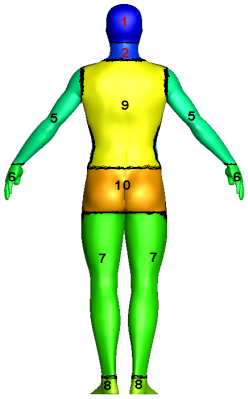

(c)

Figure 4.50: The human form decomposed into eleven body parts (and the index associated with each part).

Chapter 5

Conclusions

The URANS approach in conjunction with EIM is used here to perform the numerical simulations of aerosol particle deposition on a realistic human form. Numerical simulation of a two-phase turbulent impinging jet flow is used to validate the proposed numerical methodology for the prediction of the deposition density (or, equivalently, the deposition probability). The predicted deposition results for this case are compared with some experimental measurements. The results show that the standard EIM with turbulent tracking overpredicts the deposition efficiency. It is demonstrated that significantly improved predictions for the deposition efficiency can be obtained if a near-wall correction is included in the EIM.

After validation of the numerical methodology, detailed numerical simulations of aerosol particle deposition on a human form are conducted. The aerosol particle sizes used in these simulations cover the range from about 0.1 μm to about 40 μm. For each particle size, three different orientations of the human with respect to the incident wind direction have been simulated (namely, a human form oriented at 0, 90, and 180 degrees with respect to the direction of the incoming wind). The detailed isopleths of the deposition probability on the surface of the human form have been plotted and the associated data sets have been archived for future application. To provide the quantitative information for the future applications of these data sets by various researchers, the human form has been decomposed into eleven body parts. The association of a body part index with each triangular cell used in the tessellation of the surface of the human form has also been provided in the data files of the deposition probability.

Appendix

C source code to read the deposition results on the human:

```
#include <stdlib.h>
#include <stdio.h>
#include <math.h>
void main()
{
/*
VARIABLES:
ncells: the total number of cells;
cell_area: the area of each cell;
cell_index:
1. head (entire)
2. neck (entire)
3. upper chest (including shoulders and down to just below the nipples)
4. lower abdomen (including stomach and down to the waist)
5. arms (both left and right)
6. hands (left and right)
7. legs (left and right, front and back)
8. feet (left and right)
9. back
10. buttocks
11. crotch area (frontal area below the waist)
deposition_probability: deposition probability in each cell
*/
    double *cell_area,*deposition_probability;
    int i,id,ncells,*cell_index;
    FILE *fp;
    fp=fopen("human_results.dat","r");
    fscanf(fp,"%d",&ncells);
    cell_area=(double*)malloc(ncells*sizeof(double));
    cell_index=(int*)malloc(ncells*sizeof(int));
```

```
    deposition_probability=(double*)malloc(ncells*sizeof(double));
    for(i=0; i<ncells; i++)
    {
        fscanf(fp,"%d,%le,%d,%le",&id,&cell_area[i],&cell_index[i],&deposition_probability[i]
    }
    fclose(fp);
}
```

References

[1] J.B. McLaughlin, Aerosol Particle Deposition in Numerically Simulated Channel Flow, Phys. Fluids A, 1 (1989) 1211-1224.

[2] W.S.J. Uijttewaal and R.V.A. Oliemans, Particle Dispersion and Deposition in Direct Numerical and Large Eddy Simulations of Vertical Pipe Flows, Phys. Fluids, 8 (1996) 2590-2604.

[3] Q. Wang and K.D. Squires, Large Eddy Simulation of Particle Deposition in a Vertical Turbulent Channel Flow, Int. J. Multiphase Flow, 22 (1996) 667-683.

[4] I. Kim, S. Elgobashi and W.A. Sirignano, On the Equation for Spherical-Particle Motion: Effect of Reynolds and Acceleration Numbers, J. Fluid Mech., 367 (1998) 221-253.

[5] E.A. Matida, K. Nishino, K. Torri, Statistical Simulation of Particle Deposition on the Wall from Turbulent Dispersed Pipe Flow, Int. J. Heat Mass Transfer, 21 (2000) 389-402.

[6] D.I. Graham and P.W. James, Turbulent Dispersion of Particles Using Eddy Interaction Models, Int. J. Multiphase Flow, 22 (1996) 157-175.

[7] L.P. Wang and D.E. Stock, Stochastic Trajectory Models for Turbulent Diffusion: Monte Carlo Process Versus Markov Chains, Atmospheric Environment, 26 (1992) 1599-1607.

[8] W.H. Finlay, The Mechanics of Inhaled Pharmaceutical Aerosols, Academic Press (2001).

[9] R. Mei, Velocity Fidelity of Flow Tracer Particles, Exp. Fluids, 22 (1996) 1-13.

[10] E. Alatawi, Particulate Deposition Prediction of Diluted Two-Phase Impinging Jet, PhD Thesis, Carleton University (2013).

[11] G.A. Kallio and M.W. Reeks, A Numerical Simulation of Particle Deposition in Turbulent Boundary Layers, Int. J. Multiphase Flow, 15 (1989) 433-446.

[12] W. Burwash, W. Finlay and E. Matida, Deposition of Particles by a Confined Impinging Jet onto a Flat Surface at Re=10000, Aerosol Sci. and Technol., 40 (2006) 147-156.

[13] Y. Wang, P.W. James, On the effect of anisotropy on the turbulent dispersion and deposition of small particles, International Journal of Multiphase Flow, 25 (1999) 551-558.

[14] F.S. Lien and M.A. Leschziner, A General Non-Orthogonal Collocated Finite Volume Algorithm for Turbulent Flow at all Speeds Incorporating Second-Moment Closure, Part 1: Computational Implementation, Comp. Meth. Appl. Mech. Eng., 114 (1994) 123-148.

[15] F.S. Lien and M.A. Leschziner, Upstream Monotonic Interpolation for Scalar Transport with Application in Complex Turbulent Flows, Int. J. Num. Meth. Fluids, 19 (1994) 527-548.

[16] B.P. Leonard, A Stable and Accurate Convection Modelling Procedure Based on Quadratic Upstream Interpolation, Comput. Meth. Appl. Mech. Eng., 19 (1979) 59-98.

[17] S.V. Patankar, Numerical Heat Transfer and Fluid Flow, McGraw-Hill (1980).

[18] H. L. Stone, Iterative Solution of Implicit Approximations of Multidimensional Partial Differential Equations, SIAM J. Numer. Anal., 5, 530–558.

[19] C.M. Rhie and W.L. Chow, A Numerical Study of the Turbulent Flow Past an Isolated Airfoil with Trailing Edge Separation, AIAA J., 21 (1983) 1525-1532.

[20] M. J. Aftosmis, M. J. Berger and J. E. Melton, Robust and Efficient Cartesian Mesh Generation for Component Based Geometry, Tech. Report AIAA-97-0196, U.S. Air Force Wright Laboratory (1997).

[21] B. E. Launder, D. B. Spalding, The Numerical Computation of Turbulent Flows, Comp. Meth. Appl. Mech. Eng., 3 (1974), 1112–1128.